

**ADVANCING SUPER RESOLUTION MICROSCOPY FOR  
QUANTITATIVE IN-VIVO IMAGING OF CHROMATIN  
NANODOMAINS**

by

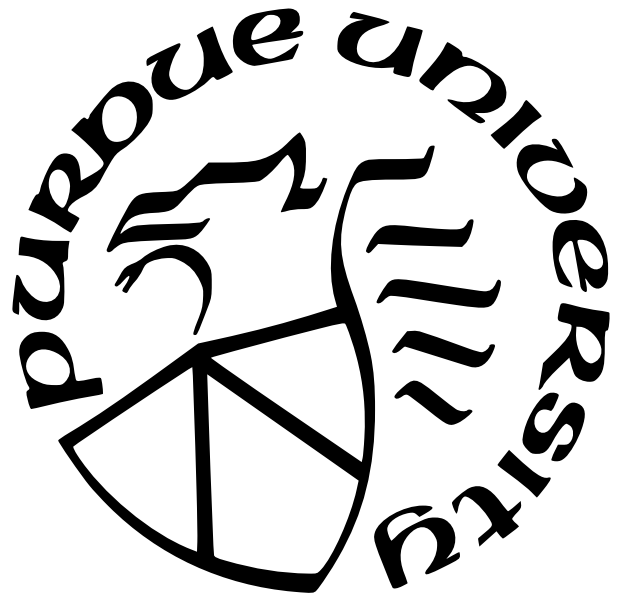
**Clayton Seitz**

**A Dissertation**

*Submitted to the Faculty of Purdue University*

*In Partial Fulfillment of the Requirements for the degree of*

**Doctor of Philosophy**



Department of Physics

Indianapolis, Indiana

December 2024

**THE PURDUE UNIVERSITY GRADUATE SCHOOL  
STATEMENT OF COMMITTEE APPROVAL**

**Dr. Gautam Vemuri, Chair**

Department of Physics

**Dr. Jing Liu**

Department of Physics

**Dr. Ruihua Cheng**

Department of Physics

**Dr. Stephen Wassall**

Department of Physics

**Dr. Horia Petrache**

Department of Physics

**Approved by:**

TBD

I dedicate this thesis to those who have encouraged my pursuit of a doctoral degree.

*To deal with a 14-dimensional space, visualize a 3-dimensional space and say 'fourteen' to yourself very loudly. Everyone does it*

Geoffrey Hinton

*Information is the resolution of uncertainty*

Claude Shannon

## **ACKNOWLEDGMENTS**

## TABLE OF CONTENTS

LIST OF TABLES . . . . .	8
LIST OF FIGURES . . . . .	9
LIST OF SYMBOLS . . . . .	11
ABSTRACT . . . . .	13
1 Single molecule localization microscopy . . . . .	14
1.1 Introduction . . . . .	14
1.1.1 Breaking the diffraction barrier . . . . .	14
1.1.2 Biological discovery with fluorescence nanoscopy . . . . .	15
1.1.3 Nanoscopy in the study of chromatin organization . . . . .	18
1.2 The Image Likelihood . . . . .	18
1.2.1 Maximization of density, minimization of error . . . . .	21
1.2.2 Thesis . . . . .	22
2 Variational Bayesian Fluorescence Nanoscopy . . . . .	24
2.1 Background . . . . .	24
2.1.1 The Bayesian calculation . . . . .	24
2.1.2 The curse of dimensionality . . . . .	26
2.1.3 The Hierarchical Variational Autoencoder . . . . .	27
2.2 Abstract . . . . .	28
2.3 Introduction . . . . .	28
2.4 Background . . . . .	30
2.4.1 Gaussian kernel density estimation . . . . .	30
2.5 Uncertainty-Aware Localization Microscopy by Variational Diffusion . . . . .	31
2.5.1 Problem Statement . . . . .	31
2.5.2 Variational Diffusion . . . . .	32
2.6 Experiments . . . . .	34

2.7	Conclusion . . . . .	36
2.8	Broader Impact . . . . .	37
2.9	Appendix . . . . .	37
2.9.1	Sampling . . . . .	37
2.9.2	Derivation of the variational bound . . . . .	38
2.9.3	Metropolis-Hastings MCMC . . . . .	40
2.9.4	Cramer-Rao Lower Bound . . . . .	41
2.9.5	Neural Networks $\psi, \phi$ . . . . .	41
3	Quantum enhanced localization with a single photon avalanche diode array . . . . .	44
3.1	Background . . . . .	44
3.1.1	A brief introduction to quantum optics . . . . .	44
3.1.2	Photon statistics . . . . .	45
3.2	Abstract . . . . .	46
3.2.1	Introduction . . . . .	46
3.2.2	Basic Scheme . . . . .	49
3.2.3	Results . . . . .	53
3.2.4	Discussion . . . . .	55
4	Fluorescence nanoscopy in the study of chromatin organization . . . . .	57
4.1	Background . . . . .	57
4.1.1	Labeling strategies of chromatin . . . . .	58
4.1.2	Chromatin-Associated Protein-Based Labeling Strategies . . . . .	58
4.1.3	DNA-Based Labeling Strategies . . . . .	59
Non-sequence Specific . . . . .	59	
Sequence Specific . . . . .	59	
4.1.4	Instrumentation for Intranucleus Imaging . . . . .	61
4.1.5	Trajectory linking . . . . .	64
4.1.6	Quantitative Analysis of Particle Motion . . . . .	65
4.1.7	Polymer Models for Chromatin Dynamics . . . . .	66
4.1.8	Super resolution of chromatin nanodomains . . . . .	67

4.2	Introduction . . . . .	67
4.3	Results . . . . .	69
4.3.1	Colocalization of BRD4 mutants with nucleosome nanodomains . . .	69
4.3.2	Chromatin structure and dynamics . . . . .	69
4.3.3	Heteropolymer model . . . . .	70
4.4	Discussion . . . . .	73
4.5	Materials and Methods . . . . .	74
4.5.1	Cell lines, cell culture conditions, and transfection . . . . .	74
4.5.2	Super-resolution imaging of nucleosome nanodomains in living cells .	74
4.5.3	Colocalization of BRD4 mutants with nucleosome nanodomains . . .	75
4.5.4	Single molecule tracking . . . . .	76
4.5.5	Immunofluorescence . . . . .	76
4.5.6	Immunoblotting . . . . .	76
	REFERENCES . . . . .	78

## **LIST OF TABLES**

## LIST OF FIGURES

1.1 <b>Stochastic optical reconstruction microscopy (STORM).</b> (A) Single molecules are resolved by separating their fluorescent emission in time, using fluorophores with multiple photophysical states (B) Example super-resolution image of H2B protein in a living Hela cell nucleus at 37C, 5 percent CO <sub>2</sub> . Image reconstructed from 10 <sup>3</sup> 10ms frames. Scalebar 5um. . . . .	17
1.2 Photoswitching of JF646 bound to H2B-HaloTag. (a) Peak intensity fluctuations of a putatively isolated JF646 molecule excited at 640nm and imaged with 10ms exposure time in the presence of 100mM MEA buffer. Fit of a Poisson HMM is shown in cyan (b) ON and OFF state lifetime distributions found by pooling data from 16 JF646 spots in a single HeLa cell nucleus. Single component exponential fits shown as solid lines. . . . .	18
1.3 . . . . .	19
1.4 <b>Noise model for CMOS cameras used for MLE.</b> (left)) CMOS offset for zero incident photons (middle) CMOS variance for zero incident photons (upper right) Cumulative mass function for the convolution distribution and its Poisson approximation for rate parameter $\mu_k = 500$ counts (lower right) Komogonov distance measured as a function of rate parameter $\mu_k$ . . . . .	20
1.5 <b>Noise model for CMOS cameras used for MLE.</b> (left)) CMOS offset for zero incident photons (middle) CMOS variance for zero incident photons (upper right) Cumulative mass function for the convolution distribution and its Poisson approximation for rate parameter $\mu_k = 500$ counts (lower right) Komogonov distance measured as a function of rate parameter $\mu_k$ . . . . .	21
2.1 . . . . .	27
2.2 Estimation of the marginal variances $\sqrt{\text{Var}(\mathbf{y}_k)}$ for an isolated fluorescent emitter. MCMC sampling is carried out using the low-resolution image (left) to estimate the posterior $p(\theta \mathbf{x})$ (middle) which is sampled $\theta \sim p(\theta \mathbf{x})$ and combined with (3) to estimate marginal variances (right) . . . . .	30
2.3 Non cherry-picked estimation of marginal variances. A low-resolution image $\mathbf{x}$ (left column) is transformed by $\phi$ to produce a KDE estimate $\hat{\mathbf{y}}$ (middle column) and a DDPM $\psi$ computes a map of marginal variances (right column) . . . . .	35
2.4 Localization errors of the trained model $\phi$ . The Cramer-Rao lower bound is shown in red, computing by taking the diagonal elements of $I^{-1}(\theta)$ . . . . .	42
3.1 . . . . .	47
3.2 . . . . .	48

3.3	Single photon counting with a SPAD array (a) Conventional widefield microscopy with integrated SPAD array (b) Single photon imaging scheme using 1us exposures containing a picosecond laser pulse (c) Sum of photon counts over a 5x5 region of interest (ROI), taken with $N_{\text{frames}} = 5 \times 10^5$	49
3.4	.....	51
3.5	Single and multi-emitter localization error on sums of photon counts. (left) Localization uncertainty for simulated data for different values of $N$ , plotted with respect to the Cramer-Rao lower bound, shown in dashed gray. (right) Multi-emitter localization by MCMC sampling for $N = 3$ , colors indicate a cluster of samples i.e., a single localization. All data was generated with a background rate $\langle \mathbf{n}_{\text{background}} \rangle = \lambda N_{\text{frames}} / d^2$ per pixel. Scalebar 360nm	52
3.6	Posteriors on the number of fluorescent emitters $N$ and localization for $N^* = 1$ (left) and $N^* = 2$ (right) quantum dots. Scalebars 360nm	53
3.7	.....	54
4.1	.....	70
4.2	.....	71
4.3	.....	72
4.4	.....	73

## LIST OF SYMBOLS

$\mathbf{x}$	An image at base resolution
$\mathbf{y}$	An image at higher resolution
$\delta$	Pixel lateral width
$k$	Pixel index
$\theta$	A parameter
$u, v$	Cartesian coordinates in two-dimensions
$g_k$	Pixel-wise gain
$o_k$	Pixel-wise offset
$w_k$	Pixel-wise readout noise standard deviation
$\mu_k$	Pixel-wise expected value
$s_k$	Pixel-wise measured signal
$\xi_k$	Pixel-wise measured readout noise
$O$	Point spread function
$\text{erf}$	Error function
$\sigma_{\mathbf{x}}$	Gaussian PSF width
$\sigma_{\mathbf{y}}$	Kernel width for kernel density estimate
$\epsilon$	An image of pure Gaussian noise
$\beta$	Diffusion model noise variance
SNR	Diffusion model signal to noise ratio
$\psi$	Diffusion model parameters
$\phi$	Augmentation network parameters
$\mathcal{L}$	An objective function
$D_{KL}$	KL-divergence
$p$	A discrete or continuous probability distribution
$\mathbb{E}_p$	Expectation with respect to a distribution $p$
$I$	Fisher information matrix
$\lambda$	Expected number of background counts per frame
$d$	Lateral dimension of a region of interest

$\zeta$	Photon detection probability
$\tau$	Delay time
$g^{(2)}(\tau)$	Second order coherence function
$B$	Expected number of signal-background coincidences per frame
$G^{(2)}(m)$	Measured number of signal-signal coincidences at lag time $m$
$N_{\text{frames}}$	Number of frames
$N$	Number of active fluorescent emitters
$N^*$	Maximum a posteriori estimate of number of active emitters
$n$	Number of photon counts in a frame
$\ell$	Log-likelihood
$\hat{a}$	Ladder operator
$\hat{E}$	Electric field operator
$\rho$	Density matrix or number density for molecular dynamics
$L(r)$	Besag's L-function
$K(r)$	Ripley's K-function
$G(r)$	Nearest neighbor distribution function
$\lambda$	(Point Pattern Analysis) Intensity of a point process
$\gamma$	Friction tensor
$\xi$	A delta-correlated Gaussian noise
$k_B$	Boltzmann's constant
$T$	Temperature
$U$	Potential energy
$D$	Diffusion coefficient
$\epsilon$	(Molecular Dynamics) Energy
$r_0$	Harmonic bond equilibrium length
$R_0$	Binder potential equilibrium length
$\alpha$	Anomalous diffusion exponent

## ABSTRACT

Single-molecule localization microscopy (SMLM) techniques, such as direct stochastic optical reconstruction microscopy (dSTORM), can be used to produce a pointillist representation of fluorescently-labeled biological structures at diffraction-unlimited precision. Direct STORM approaches leverage the deactivation of standard fluorescent tags, followed by spontaneous or photoinduced reactivation, allowing resolution of fluorophores at distances below the diffraction limit. This dissertation introduces single molecule localization microscopy and covers its application as discussed in the following papers:

*BRD4 phosphorylation regulates structure of chromatin nanodomains* [1] describes the role of the BRD4 phosphoswitch in the maintenance of chromatin nanodomains via super resolution microscopy and molecular dynamics simulation. We build on the notion that chromatin binding activity of BRD4 is regulated by phosphorylation by demonstrating that BRD4 phosphorylation regulated chromatin packing and mobility in mammalian nuclei.

*Uncertainty-aware localization microscopy by variational diffusion* [2] describes a novel algorithm that leverages a diffusion model in order to model a posterior distribution on super-resolution localization microscopy images. Fast extraction of physically relevant information from images using deep neural networks has led to significant advances in fluorescence microscopy and its application to the study of biological systems. For example, the application of deep networks for kernel density (KD) estimation in single molecule localization microscopy (SMLM) has accelerated super-resolution imaging of densely-labeled structures in the cell. However, simple and interpretable uncertainty quantification is lacking in these applications, and remains a necessary modeling component in high-risk research. We propose a generative modeling framework for KD estimation in SMLM based on variational diffusion. This approach allows us to probe the structure of the posterior on KD estimates, creating an additional avenue toward quality control. We demonstrate that data augmentation with traditional SMLM architectures followed by a diffusion process permits simultaneous high-fidelity super-resolution with uncertainty estimation of regressed KDEs.

## 1. Single molecule localization microscopy

### 1.1 Introduction

#### 1.1.1 Breaking the diffraction barrier

In the quest to understand cellular function, biologists aim to directly observe the processes enabling cells to maintain homeostasis and respond dynamically to internal and environmental cues at the molecular level. However, the inherent limitations imposed by diffraction have historically constrained the resolution achievable with conventional light microscopy. The diffraction limit, first described by Ernst Abbe in the 19th century, dictates that the resolution of a microscope is fundamentally limited by the wavelength of light used for imaging. This means that objects closer than approximately half the wavelength of light cannot be distinguished as separate entities. For visible light, this translates to a resolution limit of about 200-250 nanometers, which is insufficient for resolving many subcellular structures and molecular complexes.

Super-resolution (SR) microscopy techniques have emerged as a pathway to observing subcellular structures and dynamics with enhanced resolution, surpassing the classical Abbe diffraction limit:  $\lambda/2NA$  where  $\lambda$  is the emission wavelength and NA is the numerical aperture of an objective lens. Fluorescence microscopy techniques continually push the resolution boundary towards nanometer scales, facilitating imaging of cellular structures with a level of detail previously achievable only with electron microscopy. Concurrently, SR techniques retain optical microscopy advantages in biological experiments, including sample preservation, imaging flexibility, and target specificity. SR enables extraction of quantitative information on spatial distributions and often absolute numbers of proteins, nucleic acids, or other macromolecules within subcellular compartments. [1]

A host of SR methods have been developed in recent years, which fundamentally differ in how fluorescently labeled samples are excited and how the emitted photons are detected. Here, I focus on single-molecule localization microscopy (SMLM), also called nanoscopy, techniques. This class of diffraction-unlimited SR methods leverage fluorescence intermittency to resolve fluorophores in the sample whose spatially overlapping point spread functions would otherwise render them unresolvable at the detector. Nanoscopy approaches, such as

direct-STORM (dSTORM) have become quite popular because they can be implemented at low cost on conventional, camera-based, wide-field setups, shifting the complexity to biological sample preparation and image post processing. Common strategies for the temporal separation of molecules involve transient intramolecular rearrangements to switch from dark to fluorescent states or the exploitation of non-emitting molecular radicals. For example, in dSTORM, rhodamine derivatives can undergo intersystem crossing to a triplet state, which can be reduced by thiols to form a dark radical species. The dark state can then be quenched by oxidative processes, driving the fluorophore back to its ground state.

In nanoscopy applications, we seek the position and intensity of isolated fluorophores as well as to estimate the accuracy and precision of these parameters. Accuracy is a measure of the systematic error or bias, and precision is a measure of the statistical error of an estimator. To generate super-resolution images using SMLM, single emitters are located, and using the mosaic of their found positions, we produce a kernel density estimate (KDE). Such KDEs are often Gaussian, and are used to generate the final super-resolution images. The width of one such placed Gaussian function,  $\sigma$  is given by the precision of the fluorophore position localization. Therefore, in SMLM, it is necessary to both find the parameters and estimate their precision. Reported values are in the range of 2070 nanometers. In the following section, we derive a fundamental statistical description of fluorophore detection in SMLM, which is compatible with a coherent state of the quantized electromagnetic field. This description is necessarily simplified - background rates of light detection may vary across the field of view, and the fluorophore emission rate of chemically identical fluorophores can vary owing to effects such as uneven illumination profile, dipole orientation or different optical path lengths.

### 1.1.2 Biological discovery with fluorescence nanoscopy

The emergence of fluorescence nanoscopy has marked a significant leap forward in cell biology, enabling researchers to visualize cellular structures with unprecedented clarity and detail. This technological advancement has broken through the limitations of traditional light microscopy, which is constrained by the diffraction limit of light. As a result, sci-

tists can now explore the nanoscale organization of cells and their components, leading to groundbreaking discoveries and new insights into cellular processes.

In the early stages, most nanoscopy studies focused on mammalian cells cultured on flat surfaces, which provided a controlled environment for imaging. These initial studies revealed intricate details of cellular structures, such as organelles and protein complexes, that were previously obscured by the diffraction limit. However, as nanoscopy techniques evolved, researchers began to extend their investigations to more complex and biologically relevant systems. One significant advancement has been the application of nanoscopy to 3D cell cultures, which better mimic the *in vivo* environment compared to traditional 2D cultures. This has allowed scientists to study cellular interactions and spatial arrangements in a more realistic context. For example, researchers have used nanoscopy to examine the organization of cells within tissue constructs and to investigate the architecture of tissue microenvironments, providing new insights into tissue development and disease.

In immunology, nanoscopy has been employed to study the spatial organization of immune receptors and signaling molecules on the surface of immune cells. This has revealed new insights into how immune cells recognize and respond to pathogens. For example, super-resolution imaging of T-cell receptors has shown how these molecules cluster upon activation, providing a better understanding of the immune response at a molecular level. Nanoscopy has also proven invaluable in microbiology and virology. In these fields, researchers have utilized super-resolution imaging to visualize the structures of viruses and bacteria with exceptional detail. This has led to a deeper understanding of the molecular mechanisms underlying microbial infections and has provided insights into the structure of viral capsids and bacterial surface structures. Such information is critical for developing new antiviral and antibiotic therapies.

The ability to study cellular structures at the nanoscale has also advanced our understanding of molecular machines and complexes within cells. For instance, detailed imaging of the nuclear pore complex, a crucial structure for nucleocytoplasmic transport, has revealed the precise arrangement of its constituent proteins. This has enhanced our knowledge of how the nuclear pore complex regulates the passage of molecules between the nucleus and cytoplasm, a process essential for cellular function. In cancer biology, nanoscopy has

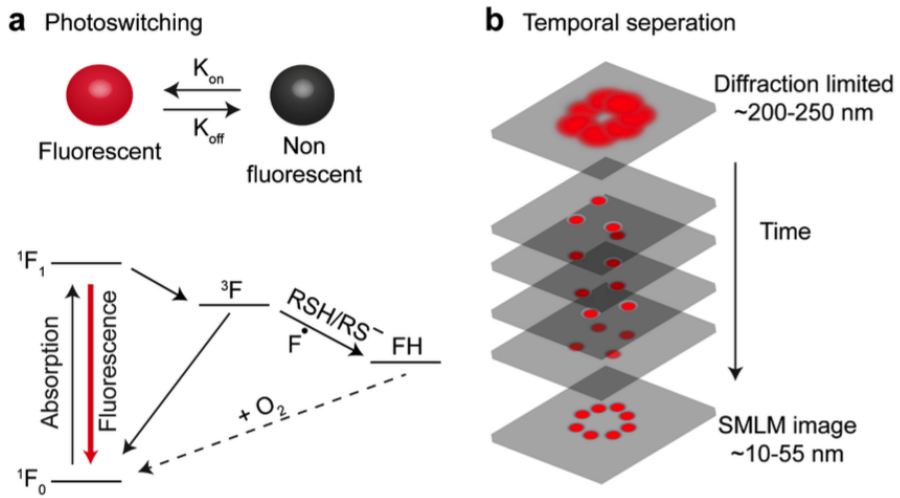


**Figure 1.1. Stochastic optical reconstruction microscopy (STORM).**

(A) Single molecules are resolved by separating their fluorescent emission in time, using fluorophores with multiple photophysical states (B) Example super-resolution image of H2B protein in a living Hela cell nucleus at 37C, 5 percent CO<sub>2</sub>. Image reconstructed from 10<sup>3</sup> 10ms frames. Scalebar 5μm.

facilitated the investigation of tumor cells and their microenvironment with unprecedented resolution. Researchers have used super-resolution techniques to study the distribution of cancer-related proteins and to understand the spatial organization of tumor cells. This has led to the identification of new biomarkers and potential therapeutic targets, offering hope for more effective cancer treatments.

As nanoscopy continues to evolve, future advancements are likely to enhance both the resolution and speed of imaging, allowing researchers to capture dynamic processes within living cells in real time. New techniques and improvements in instrumentation will expand the capabilities of nanoscopy, enabling even more detailed studies of cellular functions and interactions.

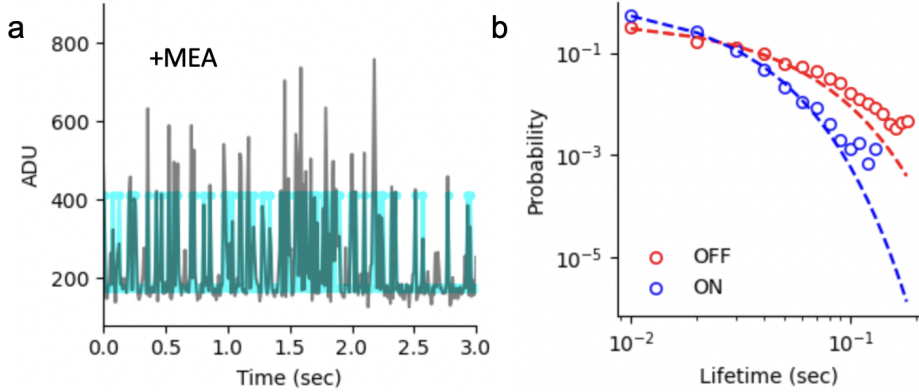


**Figure 1.2.** Photoswitching of JF646 bound to H2B-HaloTag. (a) Peak intensity fluctuations of a putatively isolated JF646 molecule excited at 640nm and imaged with 10ms exposure time in the presence of 100mM MEA buffer. Fit of a Poisson HMM is shown in cyan (b) ON and OFF state lifetime distributions found by pooling data from 16 JF646 spots in a single HeLa cell nucleus. Single component exponential fits shown as solid lines.

### 1.1.3 Nanoscopy in the study of chromatin organization

## 1.2 The Image Likelihood

It is common to describe the optical impulse response of a microscope as a two-dimensional isotropic Gaussian [2]. This is an approximation to the more rigorous diffraction models given by [3], [4]. Over a continuous domain, the impulse response reads

$$O(u, v) = \frac{1}{2\pi\sigma_x^2} e^{-\frac{(u-\theta_u)^2 + (v-\theta_v)^2}{2\sigma_x^2}}$$

The above expression can be interpreted as a probability distribution over locations where a photon can be detected. Therefore, for discrete detectors, we discretize this expression by integrating over pixels. The number of photon arrivals will follow Poisson statistics, with expected value

$$\mu_k = i_0 \left( \int_{u_k - \delta/2}^{u_k + \delta/2} O(u; \theta_u) du \right) \left( \int_{v_k - \delta/2}^{v_k + \delta/2} O(v; \theta_v) dv \right)$$

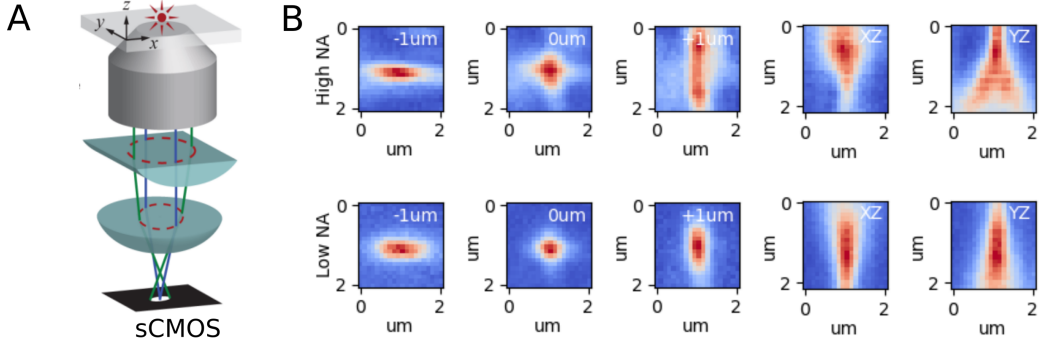


**Figure 1.3.**

The scalar quantity  $i_0$  represents the amplitude of the signal, which is proportional to the quantum efficiency of a pixel  $\eta$ , the duration of exposure,  $\Delta$ , and the number of photons emitted by a fluorescent molecule  $N_0$ . With no loss of generality,  $\Delta = \eta = 1$  and there is a single free parameter  $N_0$ . Terms above in parentheses are simply integrals of Gaussian functions and can be evaluated analytically. I define them as  $\Gamma_u, \Gamma_v$ , respectively. For example,

$$\begin{aligned} \Gamma_u &: \int_0^{u_k + \delta/2 - \theta_u} O(u) du - \int_0^{u_k - \delta/2 - \theta_u} O(u) du \\ &= \frac{1}{2} \left( \operatorname{erf} \left( \frac{u_k + \frac{\delta}{2} - \theta_i}{\sqrt{2}\sigma_x} \right) - \operatorname{erf} \left( \frac{u_k - \frac{\delta}{2} - \theta_i}{\sqrt{2}\sigma_x} \right) \right) \end{aligned}$$

where we have used the common definition  $\operatorname{erf}(z) = \frac{2}{\sqrt{\pi}} \int_0^z e^{-t^2} dt$ . Recall the central objective of SMLM is to infer a set of molecular coordinates  $\theta = (\theta_u, \theta_v)$  from measured low resolution images  $\mathbf{x}$ . In general, the likelihood on a particular pixel  $p(\mathbf{x}_k | \theta)$  is taken to be a convolution of Poisson and Gaussian distributions, due to shot noise  $p(s_k) = \text{Poisson}(\mu_k)$  and sensor readout noise  $p(\xi_k) = \mathcal{N}(o_k, w_k^2)$

$$p(\mathbf{x}_k | \theta) = A \sum_{q=0}^{\infty} \frac{1}{q!} e^{-\mu_k} \mu_k^q \frac{1}{\sqrt{2\pi} w_k} e^{-\frac{(\mathbf{x}_k - g_k q - o_k)^2}{2w_k^2}} \approx \text{Poisson}(\mu'_k) \quad (1.1)$$

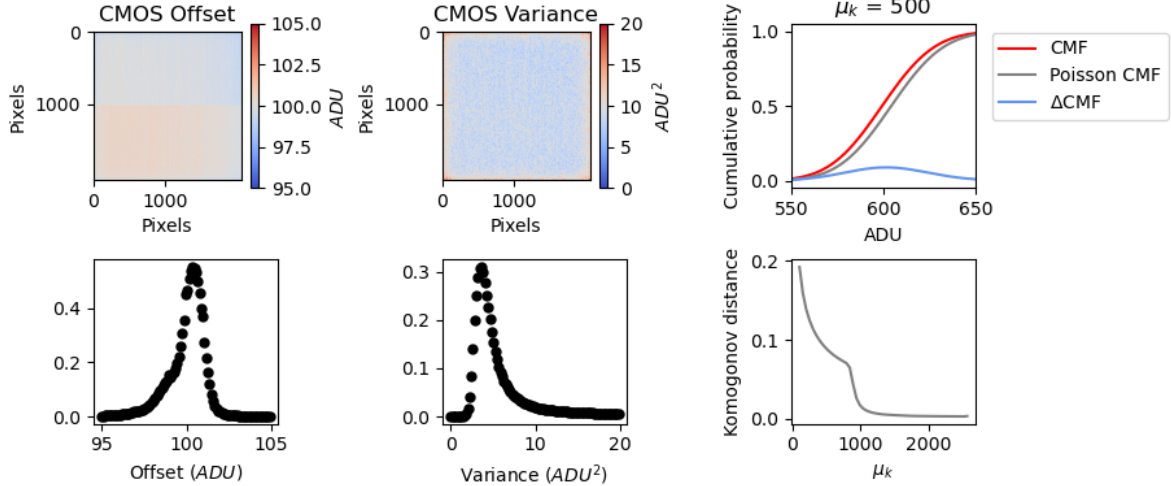


**Figure 1.4. Noise model for CMOS cameras used for MLE.** (left)) CMOS offset for zero incident photons (middle) CMOS variance for zero incident photons (upper right) Cumulative mass function for the convolution distribution and its Poisson approximation for rate parameter  $\mu_k = 500$  counts (lower right) Komogonov distance measured as a function of rate parameter  $\mu_k$

where  $A$  is some normalization constant. For the sake of generality, we include a per-pixel gain factor  $g_k$ , which is often unity. Sampling from  $p(\mathbf{x}_k|\theta)$  is trivial; however, for computation of a lower bound on uncertainty in  $\theta$ , the summation in (1) can be difficult to work with. Therefore, we choose to use a Poisson approximation for simplification, valid under a range of experimental conditions [5]. After subtraction of a known offset  $o_k$  of the pixel array, which can be easily measured, we have  $\mu'_k = \mu_k + w_k^2$ .

Under the Poisson approximation in the likelihood, the model negative log-likelihood is

$$\ell(\mathbf{x}|\theta) = -\log \prod_k \frac{e^{-(\mu'_k)} (\mu'_k)^{n_k}}{n_k!} = \sum_k \log n_k! + \mu'_k - n_k \log (\mu'_k) \quad (1.2)$$

Localization then proceeds by minimization of  $\ell(\mathbf{x}|\theta)$ .

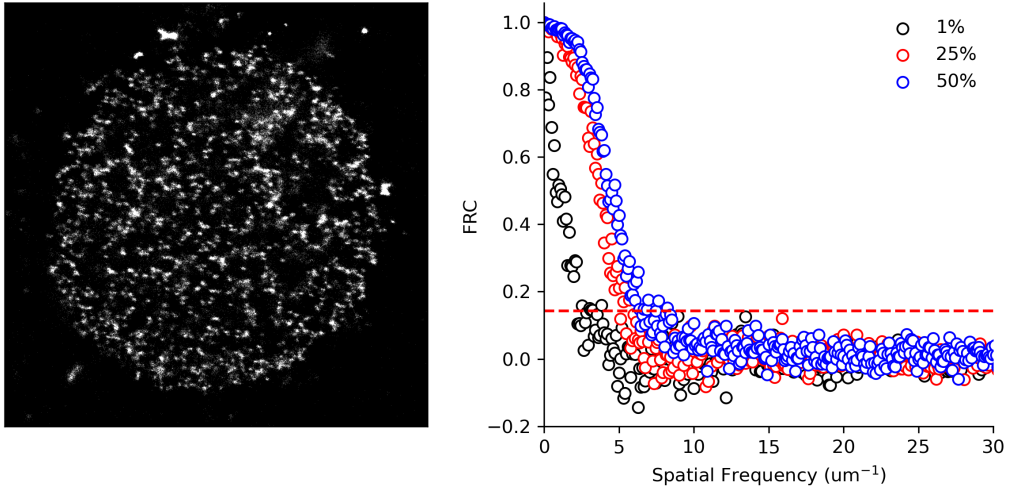


**Figure 1.5. Noise model for CMOS cameras used for MLE.** (left)) CMOS offset for zero incident photons (middle) CMOS variance for zero incident photons (upper right) Cumulative mass function for the convolution distribution and its Poisson approximation for rate parameter  $\mu_k = 500$  counts (lower right) Komogonov distance measured as a function of rate parameter  $\mu_k$

### 1.2.1 Maximization of density, minimization of error

The distribution of a particular biomolecule in the cell can be described as a probability density over a two-dimensional space, casting super-resolution as a density estimation problem. Intuitively, the spatial resolution of SMLM images then increases as we draw more samples from this density - a concept which is made mathematically precise by the so-called Fourier ring correlation or FRC. Using FRC, one can compute image resolution as the spatial frequency at which a correlation function in the frequency domain drops below a threshold, typically taken to be  $1/7$  (See Supplement). According to this theory, reducing localization uncertainty while increasing the number of samples, results in an increase in image resolution [6]. However, there remains a fundamental limit to the minimal localization uncertainty which can be obtained.

$$\text{FRC}(q) = \frac{\sum_{\vec{q} \in \text{circle}} \tilde{f}_1(\vec{q}) \tilde{f}_2(\vec{q})^*}{\sqrt{\sum_{\vec{q} \in \text{circle}} |f_1(\vec{q})|^2} \sqrt{\sum_{\vec{q} \in \text{circle}} |f_2(\vec{q})|^2}}$$

Localization uncertainty, typically the RMSE of a maximum likelihood or similar statistical estimator, is bounded from below by the inverse of the Fisher information matrix, known as the Cramer-Rao lower bound [7]. Localization uncertainties in sparse conditions are often tens of nanometers; however managing the increase in localization uncertainty at high labeling density remains a major bottleneck to SMLM. Static uncertainty due to molecular crowding can be partially ameliorated by using pairwise or higher-order temporal correlations within a pixel neighborhood, known as stochastic optical fluctuation imaging or SOFI [8]. Other approaches such as stimulated emission and depletion (STED) imaging bring control over the photophysical state of a chosen subset of the sample, yet the need for laser scanning prevents widespread application in live-cell studies. The spatial resolution and relative simplicity of SMLM techniques remains unmatched, inciting an effort to increase the resolution of SMLM techniques and explore avenues towards time resolved SMLM.

### 1.2.2 Thesis

To address the challenges posed by high-dimensional data in fluorescence nanoscopy, I propose two different methods:

The first method is model-heavy and leverages deep learning techniques. Specifically, it involves a generative modeling framework for kernel density estimation in single molecule localization microscopy, using variational diffusion. This approach not only accelerates super-resolution imaging but also provides a way to estimate uncertainty in the results.

The second method is model-light but relies on advanced hardware. This approach uses single photon avalanche diode (SPAD) arrays to accurately count active fluorescent emitters while performing intensity-based multi-emitter localization. SPAD cameras, with their high temporal resolution and single photon sensitivity, enable precise localization in non-sparse scenes.

These two methods, one focusing on sophisticated computational models and the other on cutting-edge hardware, offer complementary solutions to the high-dimensional inference

problem in super-resolution microscopy. By combining these approaches, we can achieve more accurate and reliable imaging of biological structures at the nanoscale.

## 2. Variational Bayesian Fluorescence Nanoscopy

### 2.1 Background

#### 2.1.1 The Bayesian calculation

Bayesian inference provides a rigorous framework for updating beliefs about the world in light of new data. It leverages the principles of probability theory to combine prior knowledge with empirical evidence, resulting in updated, posterior beliefs. In parametric modeling, we assume that the data  $x$  are generated from a distribution with a set of parameters  $y$ . Parametric models simplify the problem by assuming a specific form for the underlying distribution of the data, characterized by a finite set of parameters. This approach allows us to use mathematical functions to describe complex systems and make inferences about the parameters based on observed data.

At the heart of Bayesian inference is Bayes' rule, which allows us to update our beliefs based on new evidence. Bayes' rule is derived from the definition of conditional probability. The conditional probability of  $y$  given  $x$  is defined as  $P(y|x) = \frac{P(x,y)}{P(y)}$  provided that  $P(y) > 0$ . Similarly, the conditional probability of  $x$  given  $y$  is  $P(x|y) = \frac{P(x,y)}{P(x)}$ . Rearranging these equations and solving for  $P(y|x)$  gives us Bayes' rule:

$$p(y|x) = \frac{p(x|y)p(y)}{p(x)}.$$

Here,  $p(y|x)$  is the called the posterior distribution, representing our updated beliefs about the parameters after observing the data.  $p(x|y)$  is the likelihood, the probability of the observed data given the parameters.  $p(y)$  is the prior distribution, representing our beliefs about the parameters before observing the data.  $p(x)$  is the marginal likelihood or evidence, which normalizes the posterior distribution and ensures it sums to one.

One of the main challenges in Bayesian inference is the computation of the posterior distribution. The denominator in Bayes' rule,  $p(x)$ , involves an integral over all possible values of the parameters:

$$p(x) = \int p(x|y)p(y) dy.$$

In many practical applications, this integral is intractable due to the high dimensionality of the parameter space. This intractability is often referred to as the curse of dimensionality, where the complexity of computations increases exponentially with the number of dimensions. To address this challenge, various approximation methods have been developed. One such method is Markov Chain Monte Carlo (MCMC), which generates samples from the posterior distribution by constructing a Markov chain that has the desired distribution as its equilibrium distribution. MCMC methods, such as the Metropolis-Hastings algorithm and the Gibbs sampler, allow us to approximate the posterior distribution even when the exact integral is computationally infeasible.

MCMC algorithms were originally developed in the 1940s by physicists at Los Alamos. These physicists, including Ulam and Von Neumann, who were interested in modeling the probabilistic behavior of atomic particles. They could not do this analytically, but they wondered if they could use simulation. Simulation was difficult as the normalization constant was not known. Moreover, simulation as a computational tool hadn't been widely adopted yet, although ideas around simulation had been around for some time e.g., Buffon's needle (1700s), Lord Kelvin (1901), and Fermi (1930s). In fact, the term Monte Carlo was coined at Los Alamos.

Ulam and Metropolis overcame this problem by constructing a Markov chain for which the desired distribution was the stationary distribution of the Markov chain. They then only needed to simulate the Markov chain until stationarity was achieved. Towards this end, they introduced the Metropolis algorithm, and its impact was enormous. Afterwards, MCMC was introduced to statistics and generalized with the Metropolis algorithm and its variants as well as the Gibbs sampler [9]

Another approach to approximating the posterior distribution is variational inference. This method involves approximating the true posterior distribution  $p(y|x)$  with a simpler, parameterized distribution  $q(y)$  by minimizing the Kullback-Leibler (KL) divergence between them. The KL divergence  $D_{KL}(q(y)||p(y|x))$  measures how one probability distribution diverges from a second, expected probability distribution. To minimize the KL divergence, we first express it as

$$D_{KL}(q(y)|p(y|x)) = \int q(y) \log \frac{q(y)}{p(y|x)} dy.$$

This can be rewritten using Bayes' rule as

$$D_{KL}(q(y)|p(y|x)) = \int q(y) \log \frac{q(y)p(x)}{p(x|y)p(y)} dy = \log p(x) + \int q(y) \log \frac{q(y)}{p(x|y)p(y)} dy.$$

Since  $\log p(x)$  is constant with respect to  $q(y)$ , minimizing  $D_{KL}(q(y)|p(y|x))$  is equivalent to maximizing the Evidence Lower Bound (ELBO), defined as

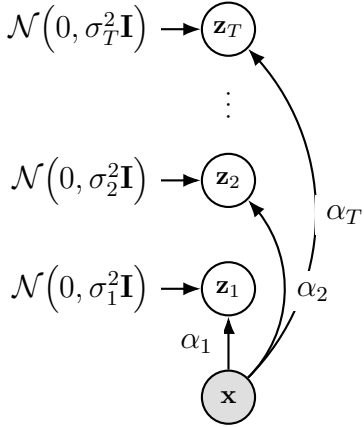
$$ELBO = \int q(y) \log \frac{p(x|y)p(y)}{q(y)} dy.$$

Maximizing the ELBO ensures that  $q(y)$  is as close as possible to the true posterior  $p(y|x)$ . This approach provides a practical way to perform Bayesian inference, especially in high-dimensional settings where traditional methods may be computationally prohibitive.

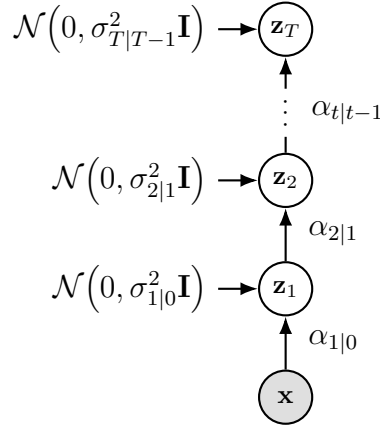
In variational inference, model parameters and latent variables can be treated interchangeably. This flexibility allows us to use powerful optimization techniques to approximate complex posterior distributions and make Bayesian inference feasible for a wide range of applications.

### 2.1.2 The curse of dimensionality

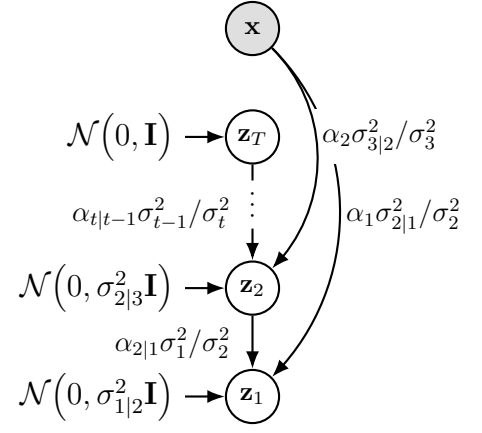
Dimensionality refers to the number of variables or features in a dataset. In fluorescence nanoscopy, each spatial coordinate (e.g., x, y, and potentially z in three-dimensional imaging) and additional attributes such as time points or different fluorophore states contribute to the dimensionality of the data. As the number of these features increases, the dataset becomes high-dimensional. The curse of dimensionality is a term coined to describe various phenomena that arise when working with high-dimensional data, making statistical analysis and machine learning more challenging. Mathematically, the curse of dimensionality can be described through the following issues:



(a) Gaussian Diffusion



(b) Markovian Transitions



(c) Top-down Posterior

Figure 2.1.

As dimensionality increases, the volume of the space grows exponentially. For instance, the volume of a hypercube with side length  $l$  in  $d$ -dimensional space is given by  $l^d$ . This rapid increase in volume means that data points become sparser, making it difficult to estimate densities and find meaningful patterns. Furthermore, in high-dimensional spaces, the concept of distance becomes less informative. For example, the difference between the minimum and maximum distance between data points tends to shrink as dimensionality increases, which can make clustering and nearest-neighbor algorithms less effective. With a large number of dimensions, models can easily become overly complex, capturing noise instead of the underlying signal. This leads to overfitting, where the model performs well on training data but poorly on unseen data. High-dimensional data requires more computational resources for processing and storage. Algorithms that are efficient in low dimensions may become impractical in high dimensions due to increased time and space complexity.

### 2.1.3 The Hierarchical Variational Autoencoder

Variational Autoencoders (VAEs), introduced by Kingma and Welling in 2013, are a sophisticated class of generative models that combine principles of variational inference with deep learning. They provide a powerful framework for learning complex, high-dimensional

data distributions by mapping data to a lower-dimensional latent space and then reconstructing the data from these latent representations. To understand VAEs, it’s essential to first appreciate their roots in Bayesian inference. Bayesian inference aims to update the probability estimate for a hypothesis as more evidence or information becomes available.

## 2.2 Abstract

Fast extraction of physically relevant information from images using deep neural networks has led to significant advances in fluorescence microscopy and its application to the study of biological systems. For example, the application of deep networks for kernel density (KD) estimation in single molecule localization microscopy (SMLM) has accelerated super-resolution imaging of densely-labeled structures in the cell. However, simple and interpretable uncertainty quantification is lacking in these applications, and remains a necessary modeling component in high-risk research. We propose a generative modeling framework for KD estimation in SMLM based on variational diffusion. This approach allows us to probe the structure of the posterior on KD estimates, creating an additional avenue toward quality control. We demonstrate that data augmentation with traditional SMLM architectures followed by a diffusion process permits simultaneous high-fidelity super-resolution with uncertainty estimation of regressed KDEs.

## 2.3 Introduction

Deep models have attracted tremendous attention from researchers in the natural sciences, with several foundational applications arising in microscopy [10], [11]. Recently, the application of deep image translation in single-molecule localization microscopy (SMLM) has received considerable interest. SMLM techniques are a mainstay of fluorescence microscopy, which localize “blinking” fluorescent molecules to produce a pointillist representation of biomolecules in the cell at diffraction-unlimited precision [12], [13]. Recently, the use of deep models to perform localization has been proposed as an alternative to traditional localization algorithms, in order to increase imaging speed and labeling density. In previous applications of deep models to localization microscopy, super-resolution images have been recovered from

a sparse set of localizations with conditional generative adversarial networks [14] or localization itself can be performed using traditional convolutional networks [15], [16]. In this paper, we perform localization indirectly by predicting kernel density (KD) estimates of a population of fluorescent molecules using a deep model.

Kernel density estimation in SMLM is necessarily performed using a single low-resolution image, and thus common measures of model performance are based on localization errors computed over ensembles of simulated images. Unfortunately, this choice precludes computation of uncertainty at test time under a fixed model. Bayesian probability theory is therefore an attractive alternative, which offers us mathematically grounded tools to reason about uncertainty.

We model a posterior on high-resolution KD estimates conditioned on a low-resolution image. Our approach is based on a type of score based generative model [17], referred to as a denoising diffusion probabilistic model (DDPM) in the literature [17], [18]. We find that this technique is complementary to relevant existing approaches to uncertainty estimation, which would primarily address epistemic sources of uncertainty, using techniques such as ensembling [19] or Monte Carlo dropout [20]. The approach is inspired by recent variational perspectives on diffusion [21]–[24]. Such techniques provide a mechanism for scalable variational inference, which can be trained using a variational bound written in terms of the signal-to-noise ratio of the diffused data, and a simple noise estimation loss. Indeed, recent efforts have shown that the variational bound can be reparameterized to give several more conventional diffusion losses [22]–[24].

In the remainder of this paper, we first introduce the likelihood of low-resolution images in localization microscopy, and show uncertainty quantification in a rudimentary example scenario. Then, we introduce KD estimation as an alternative to direct localization using low-resolution images, followed by demonstration of our variational diffusion model for measuring uncertainty KD estimation at scale.

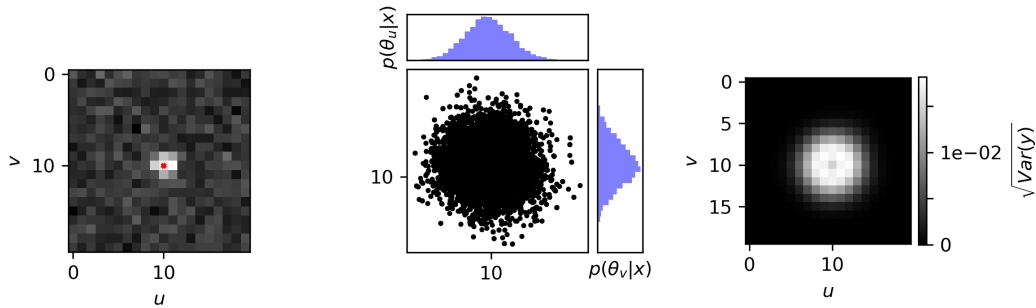


**Figure 2.2.** Estimation of the marginal variances  $\sqrt{\text{Var}(\mathbf{y}_k)}$  for an isolated fluorescent emitter. MCMC sampling is carried out using the low-resolution image (left) to estimate the posterior  $p(\theta|\mathbf{x})$  (middle) which is sampled  $\theta \sim p(\theta|\mathbf{x})$  and combined with (3) to estimate marginal variances (right)

## 2.4 Background

### 2.4.1 Gaussian kernel density estimation

Direct optimization of the likelihood in (1) from observations  $\mathbf{x}$  alone is challenging when fluorescent emitters are dense within the field of view and fluorescent signals significantly overlap. However, convolutional neural networks (CNNs) have recently proven to be powerful tools fluorescence microscopy to extract parameters describing fluorescent emitters such as color, emitter orientation,  $z$ -coordinate, and background signal [25]–[27]. For localization tasks, CNNs typically employ upsampling layers to reconstruct Bernoulli probabilities of emitter occupancy [16] or KD estimates with higher resolution than experimental measurements [15]. We choose to use KD estimates in our model, denoted by  $\mathbf{y}$ , which are latent in the low-resolution data  $\mathbf{x}$ . KDEs are the most common data structure used in SMLM, and can be easily generated from molecular coordinates, alongside observations  $\mathbf{x}$ .

Similar to the generative process on low resolution images  $\mathbf{x}$ , we generate KDEs  $\mathbf{y}$  by repurposing the generative model (1) on an unsampled image without noise. In other words, we cast Gaussian KD estimation as a noiseless image generation process on the domain of  $\mathbf{y}$ . Under a fixed configuration of  $N$  particles  $\theta$ , the value of an non-normalized KDE pixel  $\mathbf{y}_k$  is given by

$$\mathbf{y}_k(\theta) = \sum_{n=1}^N \Delta E_u(u_k, \theta_u, \sigma_y) \Delta E_v(v_k, \theta_v, \sigma_y) \quad (2.1)$$

where the hyperparameter  $\sigma_y$  is a Gaussian kernel width.

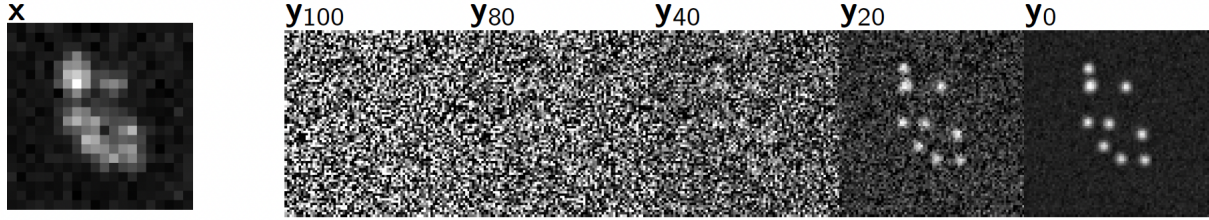
## 2.5 Uncertainty-Aware Localization Microscopy by Variational Diffusion

We now consider more realistic datasets  $(\mathbf{x}_i, \mathbf{y}_{0,i}, \hat{\mathbf{y}}_i)_{i=1}^N$  of observed images  $\mathbf{x}_i$ , true KD images  $\mathbf{y}_{0,i}$ , and augmented low-resolution inputs  $\hat{\mathbf{y}}_i = \phi(\mathbf{x}_i)$ , where  $\phi$  is a CNN. Observations  $\mathbf{x}_i$  are simulated under the convolution distribution (1) and KDEs are generated by (4).

### 2.5.1 Problem Statement

Kernel density estimates produced by the traditional deep architectures for localization microscopy produce strong results, but lack uncertainty quantification. Unfortunately, the posterior  $p(\theta|\mathbf{x})$  has no known analytical form and can be difficult to compute at test time, since (i) molecules cannot be easily resolved and therefore  $\theta$  is of unknown dimension and (ii)  $\theta$  can be high dimensional and efficient exploration of the parameter space is challenging. The central goal of this paper is to instead model a conditional distribution on the latent  $\mathbf{y}$ :  $p(\mathbf{y}|\mathbf{x})$ , where  $\mathbf{y}$  is of known dimensionality. We choose to model  $p(\mathbf{y}|\mathbf{x})$  with a diffusion model, given that the distribution  $p(\mathbf{y}|\mathbf{x})$  is expensive to compute, even if  $p(\theta|\mathbf{x})$  were known.

Recent advances in generative modeling, particularly diffusion models [17], [18] present a unique opportunity to integrate uncertainty awareness into the localization microscopy toolkit. However, sampling from diffusion models can be computationally expensive, given that generation amounts to solving a complex stochastic differential equation, effectively mapping a simple base distribution to the complex data distribution. The solution of such equations requires numerical integration with very small step sizes, resulting in thousands of neural network evaluations [28], [29]. For conditional generation tasks in high-risk applications, generation complexity is further exacerbated by the need for the highest level of detail in generated samples. Therefore, we propose that sampling is preceded by an augmentation network  $\phi$ , which in essence generates an initial estimate to guide the diffusion process. Reasoning for this choice in our application is two-fold:



**Synthesis Speed.** By training the augmentation network  $\phi$  to obtain an approximate estimate of  $\mathbf{y}_0$ , we can reduce the number of iterations, since the diffusion model only needs to model the remaining mismatch, resulting in a less complex model from which sampling becomes easier. Speed is critical in SMLM applications, which can produce thousands of images in a single experiment.

**Sample Fidelity.** Since Langevin dynamics will often be initialized in low-density regions of the data distribution, inaccurate score estimation in these regions will negatively affect the sampling process. Moreover, mixing can be difficult because of the need of traversing low density regions to transition between modes of the distribution [30].

### 2.5.2 Variational Diffusion

Diffusion models [17], [18] are a class of generative models originally inspired by nonequilibrium statistical physics, which slowly destroy structure in a data distribution via a fixed Markov chain referred to as the *forward process*. In the present context, we leverage the variational interpretation of this model class [23], [24] to approximate the posterior  $p(\mathbf{y}|\mathbf{x})$ .

**Diffusion Model.** We use a forward process which gradually adds Gaussian noise to the latent  $\mathbf{y}_0$  in discrete time, according to a variance schedule  $\beta_t$ :

$$q(\mathbf{y}_T|\mathbf{y}_0) = \prod_{t=1}^T q(\mathbf{y}_t|\mathbf{y}_{t-1}) \quad q(\mathbf{y}_t|\mathbf{y}_{t-1}) = \mathcal{N}\left(\sqrt{1 - \beta_t}\mathbf{y}_{t-1}, \beta_t I\right) \quad (2.2)$$

An important property of the forward process is that it admits sampling  $\mathbf{y}_t$  at an arbitrary timestep  $t$  in closed form [18]. Using the notation  $\alpha_t := 1 - \beta_t$  and  $\gamma_t := \prod_{s=1}^t \alpha_s$ , we have

$q(\mathbf{y}_t|\mathbf{y}_0) = \mathcal{N}(\sqrt{\gamma_t}\mathbf{y}_0, (1-\gamma_t)I)$  or  $\mathbf{y}_t = \sqrt{\gamma_t}\mathbf{y}_0 + \sqrt{1-\gamma_t}\epsilon$  for  $\epsilon \sim \mathcal{N}(0, I)$ . The signal to noise ratio (SNR) as defined in [24], at a time step  $t$  reads  $\text{SNR}_t = \gamma_t/(1-\gamma_t)$ .

The usual procedure is then to learn a parametric representation of the *reverse process*, and therefore generate samples of the latent  $\mathbf{y}_0$  from  $p(\mathbf{y}_0|\mathbf{x})$ . Formally,  $p_\psi(\mathbf{y}_0|\mathbf{x}) = \int p_\psi(\mathbf{y}_{0:T}|\mathbf{x})d\mathbf{y}_{1:T}$  where  $\mathbf{y}_t$  is a latent representation with the same dimensionality of the data and  $p_\psi(\mathbf{y}_{0:T}|\mathbf{x})$  is a Markov process, starting from a noise sample  $p_\psi(\mathbf{y}_T) = \mathcal{N}(0, I)$ . Writing this Markov process gives

$$p_\psi(\mathbf{y}_{0:T}|\mathbf{x}) = p_\psi(\mathbf{y}_T) \prod_{t=1}^T p_\psi(\mathbf{y}_{t-1}|\mathbf{y}_t, \mathbf{x}) \quad p_\psi(\mathbf{y}_{t-1}|\mathbf{y}_t, \mathbf{x}) = \mathcal{N}(\mu_\psi(\mathbf{y}_t, \gamma_t), \beta_t I) \quad (2.3)$$

where we reuse the variance schedule of the forward process [18]. From (5) it can be seen that the learnable parameter in the reverse process is the expectation of the transition  $\mu_\psi$  where  $\psi$  is a neural network.

Learning the reverse process can be approached by either regressing noise  $\epsilon$  from the forward process, or the true latent  $\mathbf{y}_0$ , as there is a deterministic relationship between them. We adopt the former for consistency with other work, and define  $\psi$  as a neural denoising function which regresses the noise  $\epsilon$  from a noisy  $\mathbf{y}_t$ . A relation between the noise estimate  $\epsilon_\psi$  and  $\mu_\psi$  is given in the Appendix, which gives an intuition for sampling. The proposed sampling scheme is depicted in (Figure 3).

**Variational Objective.** Following [23], we interpret the reverse process as a hierarchical generative model that samples a sequence of latents  $\mathbf{y}_t$ , with time running backward. Training of the model is achieved through the variational bound

$$-\log p(\mathbf{y}_0) \leq -\mathbb{E}_{q(\mathbf{y}_{1:T}|\mathbf{y}_0)} \log \left( \frac{p_\psi(\mathbf{y}_{1:T}, \mathbf{y}_0)}{q(\mathbf{y}_{1:T}|\mathbf{y}_0)} \right) \quad (2.4)$$

$$= D_{KL}(q(\mathbf{y}_T|\mathbf{y}_0)||p(\mathbf{y}_T)) + \mathbb{E}_{q(\mathbf{y}_1|\mathbf{y}_0)} \log p(\mathbf{y}_0|\mathbf{y}_1) + \mathcal{L}_\psi \quad (2.5)$$

where we have omitted conditioning on the low-resolution  $\mathbf{x}$  to simplify the notation. Note that, this is similar to a hierarchical VAE, but in a diffusion model  $q(\mathbf{y}_{1:T}|\mathbf{y}_0)$  is fixed by the forward process rather than learned. The so-called diffusion loss  $\mathcal{L}_\psi$  is shown in Appendix

$A$ , and is the term of interest as the first two terms do not contribute meaningfully to the loss [18]. Furthermore, it has become standard to use simplified forms of  $\mathcal{L}_\psi$ , such as a noise estimation loss, as this has shown superior performance. Importantly,  $\mathcal{L}_\psi$  is simply a reweighted variant of a family of diffusion objectives [23], [24]. We use the following Monte Carlo estimate of  $\mathcal{L}_\psi$ , which demonstrates that the variational bound can be written in terms of the common noise-estimation loss

$$\mathcal{L}_\psi = \mathbb{E}_{\epsilon \sim \mathcal{N}(0, I), t \sim U(1, T)} \left[ \left( \frac{\text{SNR}_{t-1}}{\text{SNR}_t} - 1 \right) \|\epsilon - \epsilon_\psi\|_2^2 \right] \quad (2.6)$$

A full derivation of this objective is outlined in the Appendix. Note that  $\text{SNR}_t$  is monotonically decreasing with  $t$ , and thus  $\frac{\text{SNR}_{t-1}}{\text{SNR}_t} = \frac{\gamma_{t-1}}{\gamma_t} \frac{1-\gamma_t}{1-\gamma_{t-1}} \geq 1$ , ensuring  $\mathcal{L}_\psi \geq 0$ . In this paper, we choose to use a uniformly weighted loss and leave the exploration of the weighted loss to future work.

## 2.6 Experiments

All training data consists of low-resolution  $20 \times 20$  images, setting  $\sigma_x = 0.92$  in units of low-resolution pixels, for consistency with common experimental conditions with a 60x magnification objective lens and numerical aperture (NA) of 1.4. We multiply  $\omega_k$  by a constant  $i_0 = 200$  for experiments for consistency with typical fluorophore emission rates. All KDEs have dimension  $80 \times 80$ , are scaled between  $[0, 1]$ , and are generated using  $\sigma_y = 3.0$  pixels in the upsampled image. For a typical CMOS camera, this results in KDE pixels with lateral dimension of  $\approx 27\text{nm}$ . Initial coordinates  $\theta$  were drawn uniformly over a two-dimensional disc with a radius of 7 low-resolution pixels.

**Localization RMSE.** In order to verify the initial predictions made by the augmentation model  $\phi$ , we simulated a dataset  $(\mathbf{x}_i, \mathbf{y}_{0,i}, \hat{\mathbf{y}}_i)_{i=1}^N$  with  $N = 1000$ . Objects in the KDE  $\hat{\mathbf{y}}_i$  are detected using the Laplacian of Gaussian (LoG) detection algorithm [1], which permits more direct comparison of model predictions to the Cramer-Rao lower bound on localization error, compared to other image similarity measures. Localization is carried out from scale-space maxima directly in LoG, as opposed to fitting a model function to KDEs. A particular LoG localization in the KDE is paired to the nearest ground truth localization

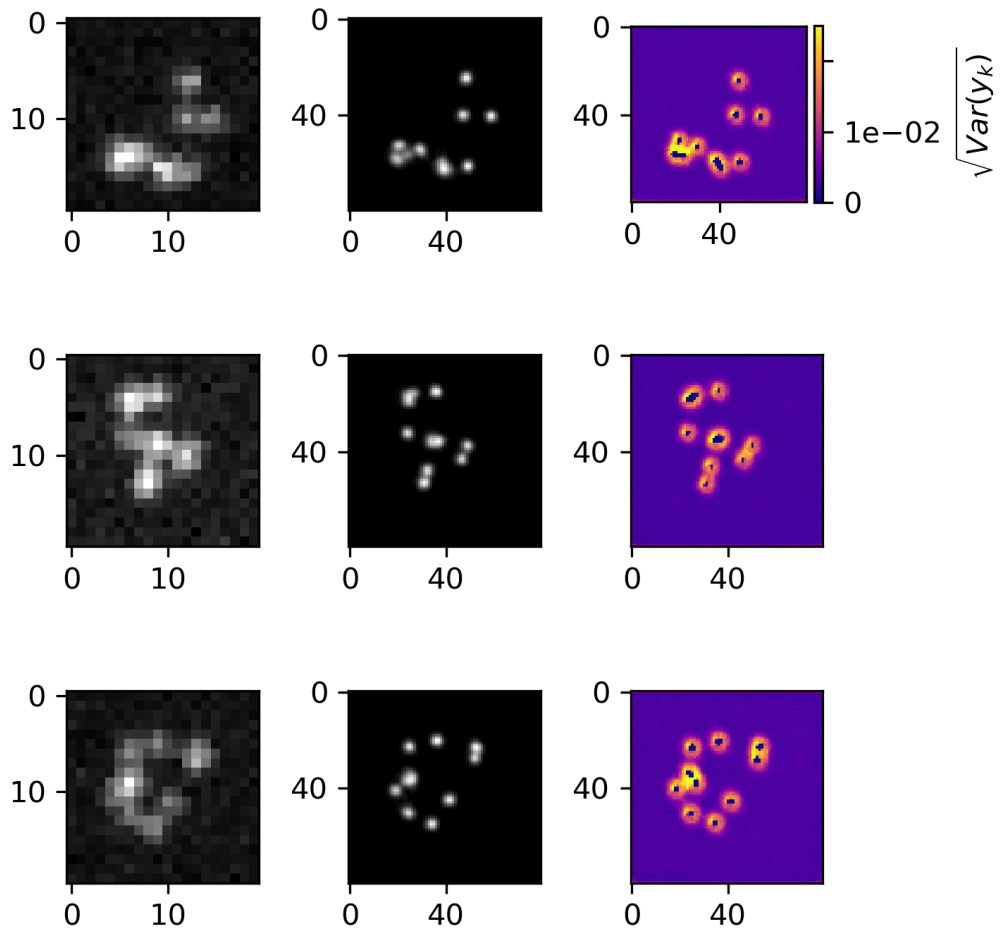


**Figure 2.3.** Non cherry-picked estimation of marginal variances. A low-resolution image  $\mathbf{x}$  (left column) is transformed by  $\phi$  to produce a KDE estimate  $\hat{\mathbf{y}}$  (middle column) and a DDPM  $\psi$  computes a map of marginal variances (right column)

and is unpaired if a localization is not within 5 KDE pixels of any ground truth localization. In addition to localization error, we measure a precision  $P = TP / (TP + FP) = 1.0$  and recall  $R = TP / (TP + FN) = 0.85$ , where TP denotes true positive localizations, FP denotes false positive localizations, and FN denotes false negative localizations.

**Variational Diffusion.** We set  $T = 100$  for all experiments and treat forward process variances  $\beta_t$  as hyperparameters, with a linear schedule from  $\beta_0 = 10^{-4}$  to  $\beta_T = 10^{-2}$ . These constants were chosen to be small relative to ground truth KDEs, which are scaled to  $[-1, 1]$ , ensuring that forward process distribution  $\mathbf{y}_T \sim q(\mathbf{y}_T | \mathbf{y}_0)$  approximately matches the reverse process  $\mathbf{y}_T \sim \mathcal{N}(0, I)$  at  $t = T$ . Example KD estimates from low-resolution images and the marginal variances obtained from sampling  $N = 100$  samples from  $p_\psi(\mathbf{y}_0 | \mathbf{x})$  are shown in (Figure 4).

## 2.7 Conclusion

We proposed a variational diffusion model for uncertainty-aware localization microscopy. Our approach builds on recent advancements in conditional diffusion models, to model the posterior distribution on high-resolution KD estimates from low-resolution inputs. This tractable posterior distribution is constructed by first augmenting low resolution inputs to a KD estimate using the DeepSTORM architecture with minor modifications [15]. Conditioning a diffusion model on this initial estimate permits sampling with relatively fewer samples than most existing diffusion models in similar applications, thereby making computation of marginal variances possible. Our approach made three core contributions: (i) we derived a relationship between the posterior on kernel density estimates with the posterior on molecular locations, and (ii) we demonstrated that a diffusion model can model a distribution on KDEs with qualitatively similar marginal variances expected from predictions made using MCMC. By using a recently discovered relationship of the variational lower bound to a traditional noise-estimation objective, we can confidently approximate the true posterior.

## 2.8 Broader Impact

The development of a method for uncertainty estimation in super-resolution imaging, as proposed here, holds implications beyond its immediate application in SMLM. By leveraging diffusion models for uncertainty estimation, this approach not only enhances the reliability of super-resolution image reconstructions but also extends its utility to a diverse array of domains. The incorporation of a guided diffusion process facilitates efficient reconstruction while maintaining interpretation of the underlying uncertainty. Importantly, the principles underlying this method resonate across various fields, suggesting its potential applicability in domains beyond microscopy. For instance, the extension of similar techniques to general image processing tasks highlights the potential to address uncertainty in a wide range of applications in bioimaging or medical imaging. Moreover, the utilization of diffusion models for uncertainty estimation aligns with a broader trend in leveraging probabilistic frameworks for enhancing deep learning applications, with implications extending to fields such as natural language processing, computer vision, and autonomous systems. By bridging these interdisciplinary boundaries, this method not only addresses a critical need in localization microscopy but also contributes to the advancement of uncertainty-aware deep learning methodologies.

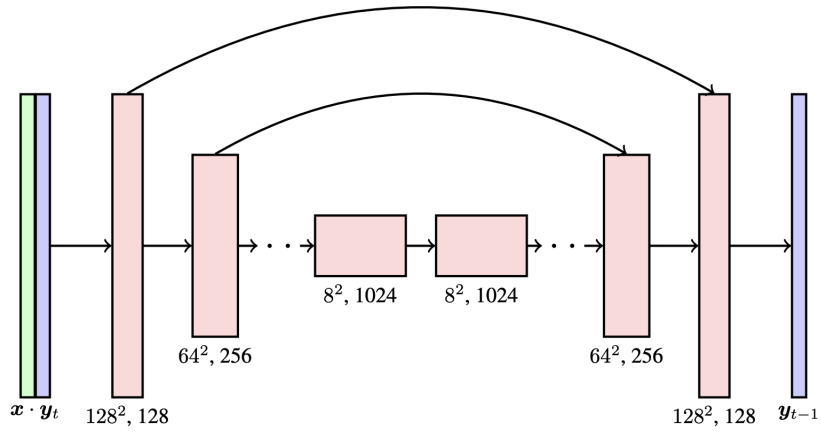
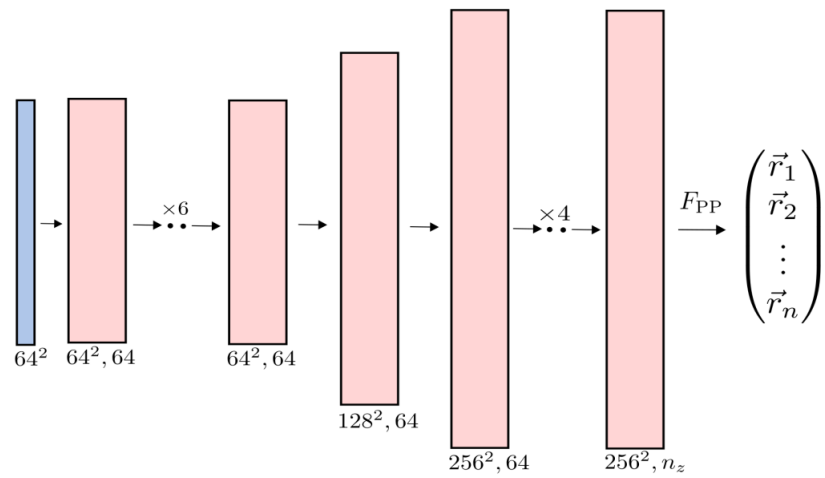
## 2.9 Appendix

### 2.9.1 Sampling

Sampling from the reverse process  $p_\psi(\mathbf{y}_{t-1}|\mathbf{y}_t, \mathbf{x})$  is achieved by estimation of the noise  $\epsilon_\psi$  from  $\mathbf{y}_t$  by the denoising model  $\psi$ , and therefore estimation of  $\mathbf{y}_0$

$$\hat{\mathbf{y}}_0 = \frac{1}{\sqrt{\gamma_t}}(\mathbf{y}_t - \sqrt{1-\gamma_t}\epsilon_\psi) \quad (2.7)$$

followed by sampling from the forward process  $\mathbf{y}_{t-1} \sim q(\mathbf{y}_{t-1}|\hat{\mathbf{y}}_0) = \mathcal{N}(\sqrt{\gamma_{t-1}}, (1-\gamma_{t-1})I)$ .



### 2.9.2 Derivation of the variational bound

We now derive the so-called diffusion loss  $\mathcal{L}_\psi$ , written in (8) in the main text. Similar derivations can be found in [22], [23], and we include it here only for completeness

$$\begin{aligned}
-\log p(\mathbf{y}_0) &\leq -\mathbb{E}_{q(\mathbf{y}_{1:T}|\mathbf{y}_0)} \log \frac{p(\mathbf{y}_{0:T})}{q(\mathbf{y}_{1:T}|\mathbf{y}_0)} \\
&= -\mathbb{E}_{q(\mathbf{y}_{1:T}|\mathbf{y}_0)} \log \frac{p(\mathbf{y}_T)p(\mathbf{y}_0|\mathbf{y}_1)\prod_{t=2}^T p(\mathbf{y}_{t-1}|\mathbf{y}_t)}{q(\mathbf{y}_T|\mathbf{y}_0)\prod_{t=2}^T q(\mathbf{y}_{t-1}|\mathbf{y}_t, \mathbf{y}_0)} \\
&= -\mathbb{E}_{q(\mathbf{y}_{1:T}|\mathbf{y}_0)} \left[ p(\mathbf{y}_0|\mathbf{y}_1) + \log \frac{p(\mathbf{y}_T)}{q(\mathbf{y}_T|\mathbf{y}_0)} + \sum_{t=2}^T \log \frac{p(\mathbf{y}_{t-1}|\mathbf{y}_t)}{q(\mathbf{y}_{t-1}|\mathbf{y}_t, \mathbf{y}_0)} \right] \\
&= -\mathbb{E}_{q(\mathbf{y}_{1:T}|\mathbf{y}_0)} [p(\mathbf{y}_0|\mathbf{y}_1)] + D_{KL}(q(\mathbf{y}_T|\mathbf{y}_0)||p(\mathbf{y}_T)) \\
&\quad + \sum_{t=2}^T \mathbb{E}_{q(\mathbf{y}_t|\mathbf{y}_0)} D_{KL}(q(\mathbf{y}_{t-1}|\mathbf{y}_t, \mathbf{y}_0)||p(\mathbf{y}_{t-1}|\mathbf{y}_t))
\end{aligned}$$

As before, we omit conditioning on  $\mathbf{x}$  to simplify the notation. The first term is typically ignored, as it does not contribute meaningfully to the loss [22]. Furthermore, the second term is approximately zero by construction. Therefore we are left with the last term, called the diffusion loss  $\mathcal{L}_\psi$ . The KL-divergence of  $q$  and  $p$  is between two Gaussians with identical variances  $\sigma^2 = \frac{(1-\gamma_{t-1})(1-\alpha_t)}{1-\gamma_t}$ , and expectations

$$\mu = \frac{\sqrt{\gamma_{t-1}}(1-\alpha_t)}{1-\gamma_t} \mathbf{y}_0 + \frac{\sqrt{\alpha_t}(1-\gamma_{t-1})}{1-\gamma_t} \mathbf{y}_t \quad \mu_\psi = \frac{\sqrt{\gamma_{t-1}}(1-\alpha_t)}{1-\gamma_t} \hat{\mathbf{y}}_0 + \frac{\sqrt{\alpha_t}(1-\gamma_{t-1})}{1-\gamma_t} \mathbf{y}_t$$

for a fixed noise schedule [28]. Therefore, we have

$$\begin{aligned}
D_{KL}(q(\mathbf{y}_{t-1}|\mathbf{y}_t, \mathbf{y}_0)||p(\mathbf{y}_{t-1}|\mathbf{y}_t)) &= \frac{1}{2\sigma^2} \|\mu - \mu_\psi\|_2^2 \\
&= \frac{1}{2} \frac{\gamma_{t-1}(1-\alpha_t)}{(1-\gamma_{t-1})(1-\gamma_t)} \|\mathbf{y}_0 - \hat{\mathbf{y}}_0\|_2^2 \\
&= \frac{1}{2} \frac{\gamma_{t-1}((1-\gamma_t) - \alpha_t(1-\gamma_{t-1}))}{(1-\gamma_{t-1})(1-\gamma_t)} \|\mathbf{y}_0 - \hat{\mathbf{y}}_0\|_2^2 \\
&= \frac{1}{2} \frac{\gamma_{t-1}((1-\gamma_t) - \frac{\gamma_t}{\gamma_{t-1}}(1-\gamma_{t-1}))}{(1-\gamma_{t-1})(1-\gamma_t)} \|\mathbf{y}_0 - \hat{\mathbf{y}}_0\|_2^2 \\
&= \frac{1}{2} \left( \frac{\gamma_{t-1}}{1-\gamma_{t-1}} - \frac{\gamma_t}{1-\gamma_t} \right) \|\mathbf{y}_0 - \hat{\mathbf{y}}_0\|_2^2 \\
&= \frac{1}{2} (\text{SNR}_{t-1} - \text{SNR}_t) \|\mathbf{y}_0 - \hat{\mathbf{y}}_0\|_2^2
\end{aligned}$$

Reparameterizing the loss in terms of the noise, using  $\|\mathbf{y}_0 - \hat{\mathbf{y}}_0\|_2^2 = \frac{1-\gamma_t}{\gamma_t} \|\epsilon_0 - \epsilon_\psi\|_2^2$  [22], we arrive at

$$\mathcal{L}_\psi = \frac{1}{2} \sum_{t=2}^T \mathbb{E}_{q(\mathbf{y}_t|\mathbf{y}_0)} \left( \frac{\text{SNR}_{t-1}}{\text{SNR}_t} - 1 \right) \|\epsilon - \epsilon_\psi\|_2^2$$

Using a Monte Carlo estimate of  $\mathcal{L}_\psi$  [24] which optimizes random terms of the summation to avoid calculating all terms simultaneously, we arrive at the objective written in the main text (8)

$$\mathcal{L}_\psi = \mathbb{E}_{\epsilon \sim \mathcal{N}(0, I), t \sim U(1, T)} \left[ \left( \frac{\text{SNR}_{t-1}}{\text{SNR}_t} - 1 \right) \|\epsilon - \epsilon_\psi\|_2^2 \right]$$

### 2.9.3 Metropolis-Hastings MCMC

To obtain numerical estimates of  $p(\theta|\mathbf{x}) \propto p(\mathbf{x}|\theta)p(\theta)$  and therefore  $p(\mathbf{y}|\mathbf{x})$ , for the isolated fluorescent molecule as shown in (Figure 2), we used Metropolis-Hastings Markov Chain Monte Carlo (MCMC) to estimate the posterior on coordinates. Under the Poisson approximation in (1), the model negative log-likelihood is

$$\ell(\mathbf{x}|\theta) = -\log \prod_k \frac{e^{-(\omega'_k)} (\omega'_k)^{n_k}}{n_k!} = \sum_k \log n_k! + \omega'_k - n_k \log (\omega'_k) \quad (2.8)$$

where  $n_k$  is the observed number events at a pixel. MCMC is asymptotically exact, which is not guaranteed by variational methods which may rely on a Laplace approximation around the MLE. We choose a uniform prior  $p(\theta)$ , and Metropolis-Hastings is run for  $10^4$  iterations, the first  $10^3$  iterations are discarded as burn-in. A proposal  $\theta' = \theta + \Delta\theta$  was generated with  $\Delta\theta \sim \mathcal{N}(0, \sigma^2 I)$  where  $\sigma^2 = 0.05$ . The acceptance probability is

$$\alpha = e^{\beta(\ell(\theta) - \ell(\theta'))}$$

We choose  $\beta = 0.2$  to achieve a target acceptance rate of 0.5.

#### 2.9.4 Cramer-Rao Lower Bound

Reliable inference of  $\theta$  from  $\mathbf{x}$  in general requires performance metrics for model selection. We use the Fisher information as an information theoretic criteria to assess the quality of the data augmentation model  $\phi$  tested here, with respect to the root mean squared error (RMSE) of our predictions of  $\theta$  [7]. The Poisson log-likelihood  $\ell(\mathbf{x}|\theta)$  is also convenient for computing the Fisher information matrix [31] and thus the Cramer-Rao lower bound, which bounds the variance of a statistical estimator of  $\theta$ , from below i.e.,  $\text{var}(\hat{\theta}) \geq I^{-1}(\theta)$ . The Fisher information is straightforward to compute under the Poisson log-likelihood in (1). In general, the Fisher information is given by the expression

$$I_{ij}(\theta) = \mathbb{E}_{\theta} \left( \frac{\partial \ell}{\partial \theta_i} \frac{\partial \ell}{\partial \theta_j} \right) \quad (2.9)$$

For an arbitrary parameter, we find that, for a Poisson log-likelihood  $\ell$

$$\begin{aligned} \frac{\partial \ell}{\partial \theta_i} &= \frac{\partial}{\partial \theta_i} \sum_k \log n_k! + \omega'_k - n_k \log (\omega'_k) \\ &= \sum_k \frac{\partial \omega'_k}{\partial \theta_i} \left( \frac{\omega'_k - n_k}{\omega'_k} \right) \end{aligned}$$

Using this result, we can compute the Fisher information matrix  $I(\theta)$

$$I_{ij}(\theta) = \mathbb{E}_{\theta} \left( \sum_k \frac{\partial \omega'_k}{\partial \theta_i} \frac{\partial \omega'_k}{\partial \theta_j} \left( \frac{\omega'_k - n_k}{\omega'_k} \right)^2 \right) = \sum_k \frac{1}{\omega'_k} \frac{\partial \omega'_k}{\partial \theta_i} \frac{\partial \omega'_k}{\partial \theta_j}$$

A fundamental lower bound on the variance in our estimates of  $\theta$  then is found from its inverse:  $\text{CRLB} = I^{-1}(\theta)$ . This result is used to show in (Figure 5), that the data augmentation model  $\phi$  efficiently estimates molecular coordinates under the experimental conditions tested here.

#### 2.9.5 Neural Networks $\psi, \phi$

**DeepSTORM CNN  $\phi$ .** The DeepSTORM CNN, for 3D localization, can be viewed as a deep kernel density estimator, reconstructing kernel density estimates  $\mathbf{y}$  from low-

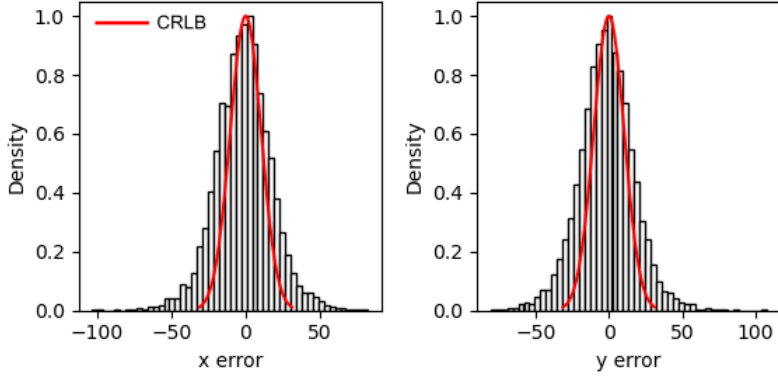


**Figure 2.4.** Localization errors of the trained model  $\phi$ . The Cramer-Rao lower bound is shown in red, computing by taking the diagonal elements of  $I^{-1}(\theta)$ .

resolution inputs  $\mathbf{x}$ . We utilize a simplified form of the original architecture [15] for 2D localization, which we denote  $\phi$  in this paper, which consists of three main modules: a multi-scale context aggregation module, an upsampling module, and a prediction module. For context aggregation, the architecture utilizes dilated convolutions to increase the receptive field of each layer. The upsampling module is then composed of two consecutive 2x resize-convolutions, computed by nearest-neighbor interpolation, to increase the lateral resolution by a factor of 4. Additional details regarding this architecture can be found in the original paper [15]. The terminal prediction module contains three additional convolutional blocks for refinement of the upsampled image, followed by an element-wise HardTanh. The architecture is trained using the objective  $\mathcal{L}_\phi = \frac{1}{N} \sum_{n=1}^N (\mathbf{y}_{0,n} - \hat{\mathbf{y}}_n)^2$ .

**DDPM  $\psi$ .** To represent the reverse process, we used a DDPM architecture originally proposed in [28]. We chose the U-Net backbone to have channel multipliers [1, 2, 4, 8, 8] in the downsampling and upsampling paths of the architecture. In this architecture, parameters are shared across time, which is specified to the network using the Transformer sinusoidal position embedding, and uses self-attention at the  $16 \times 16$  feature map resolution. To condition the model on the input  $\hat{\mathbf{y}}$ , we concatenate the  $\hat{\mathbf{y}}$  estimated by DeepSTORM along the channel dimension, which are scaled to  $[0, 1]$ , with  $\mathbf{y}_T \sim \mathcal{N}(0, I)$ . Others have experimented

with more sophisticated methods of conditioning, but found that the simple concatenation yielded similar generation quality [28].

### 3. Quantum enhanced localization with a single photon avalanche diode array

#### 3.1 Background

##### 3.1.1 A brief introduction to quantum optics

Experimental techniques have surfaced which take advantage of the quantum nature of light to enhance imaging methods. The advent of very fast and sensitive detectors allows us to measure EM fields at a timescale where quantum effects can be seen. We often speak of concepts such as photon counting or photon statistics, and it is prudent to define what a photon really is and how it be measured with this technology. Therefore, it is necessary to define a very basic formulation of the quantization of the electromagnetic field.

We start by stating the major results of quantizing the EM field at a single point in space, which could be a point detector element, for example. Quantizing the field at a single point in space simplifies the problem to focusing only on time dependence where spatial heterogeneity of the field can be ignored. We express the time-dependent field as a sum of harmonic oscillators using a Fourier series expansion. We consider an oscillation  $E(t)$  that can only exist in one dimension, or a single polarization, making the field effectively a scalar one. This decomposition represents the field in terms of an infinite number of modes indexed by  $k$  with frequency  $\omega_k$  i.e.,  $E(t) = \sum_{k=1}^{\infty} c_k e^{-i\omega_k t}$ . In order to quantize the field, each mode is treated as a quantum harmonic oscillator. As such, the Hamiltonian for one particular mode is that of a quantum harmonic oscillator which has energy eigenvalues  $E_k = \hbar\omega_k(\hat{n} + \frac{1}{2})$ . The operator  $\hat{n} = \hat{a}^\dagger \hat{a}$  is the number operator such that  $\hat{n} |\psi\rangle = n |\psi\rangle$  where  $n$  is the number of energy quanta in that particular mode. The value of  $n$  represents the number of energy quanta present in the field, each quanta being called a photon. Since there are potentially infinitely many modes, the wavefunction at this point is then  $|\psi\rangle = |n_1, n_2, \dots\rangle$  where  $n_1$  is the number of photons in the first mode,  $n_2$  is the number of photons in the second mode, and so on. The number operator for the  $n$ -th mode is  $\hat{n}_k |\psi\rangle = n_k |\psi\rangle$ .

We also define  $\hat{a}_n$  and  $\hat{a}_n^\dagger$  as the respective annihilation and creation operators for the  $n$ -th mode. These operators satisfy the commutation relations  $[\hat{a}_k, \hat{a}'_k] = \delta_{kk'}$  and  $[\hat{a}_k, \hat{a}'_k] =$

$[\hat{a}_k^\dagger, \hat{a}_k^\dagger] = 0$ . The action of the annihilation and creation operators on the joint number states is:

$$\hat{a}_k |n_1, n_2, \dots\rangle = n_k |n_1, n_2, \dots\rangle \quad \hat{a}_k^\dagger |n_1, n_2, \dots\rangle = (n + 1) |n_1, n_2, \dots\rangle$$

### 3.1.2 Photon statistics

At this point in space, we can define any  $|\psi\rangle$  that we like in this framework. However, there are certain interesting states which have special properties, such as the coherent state. Coherent states are a special class of states that resemble classical states of the EM field. Qualitatively, at a point, they would give rise to a coherent sinusoidal behavior of the field. Suppose we have a single mode field in a state  $|m\rangle$ . A coherent state  $|\alpha\rangle$  is defined as the eigenstate of the annihilation operator  $\hat{a}$ :

$$\hat{a} |\alpha\rangle = \alpha |\alpha\rangle$$

where  $\alpha$  is a complex number. The coherent states are given by:

$$|\alpha\rangle = e^{-\frac{|\alpha|^2}{2}} \sum_{m=0}^{\infty} \frac{\alpha^m}{m!} |m\rangle$$

It turns out that if we measure a number of photons (intensity) in this state, we would find that the number of photons has Poisson statistics. To see this, we calculate the probability  $P(m)$  of finding  $m$  photons in a coherent state  $|\alpha\rangle$ :

$$P(m) = |\langle m| |\alpha\rangle|^2 = |e^{-\frac{|\alpha|^2}{2}} \frac{\alpha^m}{m!}|^2 = e^{-|\alpha|^2} \frac{|\alpha|^{2m}}{m!}$$

This is simply the Poisson distribution with mean  $\langle \hat{n}_n \rangle = |\alpha|^2$ . The variance of the photon number distribution in a coherent state is also  $|\alpha|^2$ , characteristic of Poisson statistics, where the mean and variance are equal.

In contrast, single photon states e.g.,  $|1\rangle$  do not necessarily follow Poisson statistics. This state could be prepared by an isolated single photon source such as a fluorescent dye molecule which can produce only a single photon at a time. This phenomenon is referred

to as *fluorescence antibunching* where photons tend to be detected as isolated events rather than in bursts or bunches. Note that for such a single photon source the single-mode field can be in state  $|1\rangle$  but not state  $|2\rangle$  at any given time. If more single photon sources are present states beyond  $|1\rangle$  are achievable. This has led to the introduction of binomial states of the quantized field.

## 3.2 Abstract

Conventional single molecule localization microscopy infers the locations of putatively isolated fluorescent emitters to produce super-resolved images. The number of active fluorescent emitters is therefore a critical piece of information during localization; however, this quantity is generally underdetermined in widefield fluorescent microscopy. Nevertheless, many fluorophores used in bioimaging are intrinsically single photon sources which exhibit fluorescence antibunching and can emit only one photon following a very short excitation pulse. This general property may provide the necessary physical information for constrained localization in non-sparse scenes by yielding estimates of the number active fluorescent emitters. Here, we leverage recent advancements in single photon avalanche diode (SPAD) arrays to accurately count the number active emitters in a fluorescent sample, while concurrently performing intensity-based multi-emitter localization. We find that SPAD cameras, with their high temporal resolution and single photon sensitivity are capable of precise single molecule localization microscopy, while maintaining the relative simplicity of widefield imaging.

### 3.2.1 Introduction

Far-field optical microscopy is fundamentally limited by diffraction, with the maximum attainable resolution being limited to approximately half the wavelength of light. Several schemes to beat the diffraction limit have been developed in recent years. Many of these schemes utilize the concept of precise localization of isolated fluorescent emitters which blink over a time series of frames [12], [13]. An inherent problem with such methods is the requirement that fluorescent emitters be isolated, slowing down the acquisition of super-

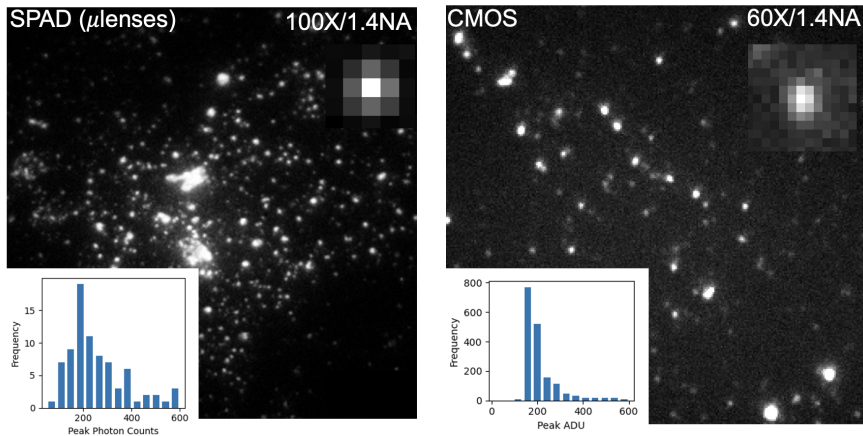


**Figure 3.1.**

resolved images. To address this, we leverage the fact that many fluorophores are intrinsically single photon sources and exhibit fluorescence antibunching. This property can constrain the number of active fluorescent emitters in a region of interest (ROI) and can potentially enable localization in non-sparse scenes [32], [33].

Molecular counting with fluorescence antibunching has a fairly simple motivation: coincidence of photons at multiple detector elements during high speed imaging provides evidence for the number of single photon sources present in the imaged region. Combining the ideas of conventional super-resolution approaches with photon statistics may prove to be a powerful set of methods for bioimaging. SPAD cameras achieve orders of magnitude higher temporal resolutions than standard CMOS cameras, single photon sensitivity, and dark count rates less than 25cps. Furthermore, the reduced readout noise and large fill-factor of recently commercialized SPAD arrays suggests their use for single molecule localization with reduced localization uncertainty. Localization uncertainty, typically the root mean square error (RMSE) of a maximum likelihood or similar statistical estimator, is bounded from below by the inverse of the Fisher information matrix, known as the Cramer-Rao lower bound [7]. Managing the increase in localization uncertainty at high labeling density remains a major bottleneck to localization microscopy. For example, static uncertainty due to molecular crowding can be partially ameliorated by using pairwise or higher-order temporal correla-

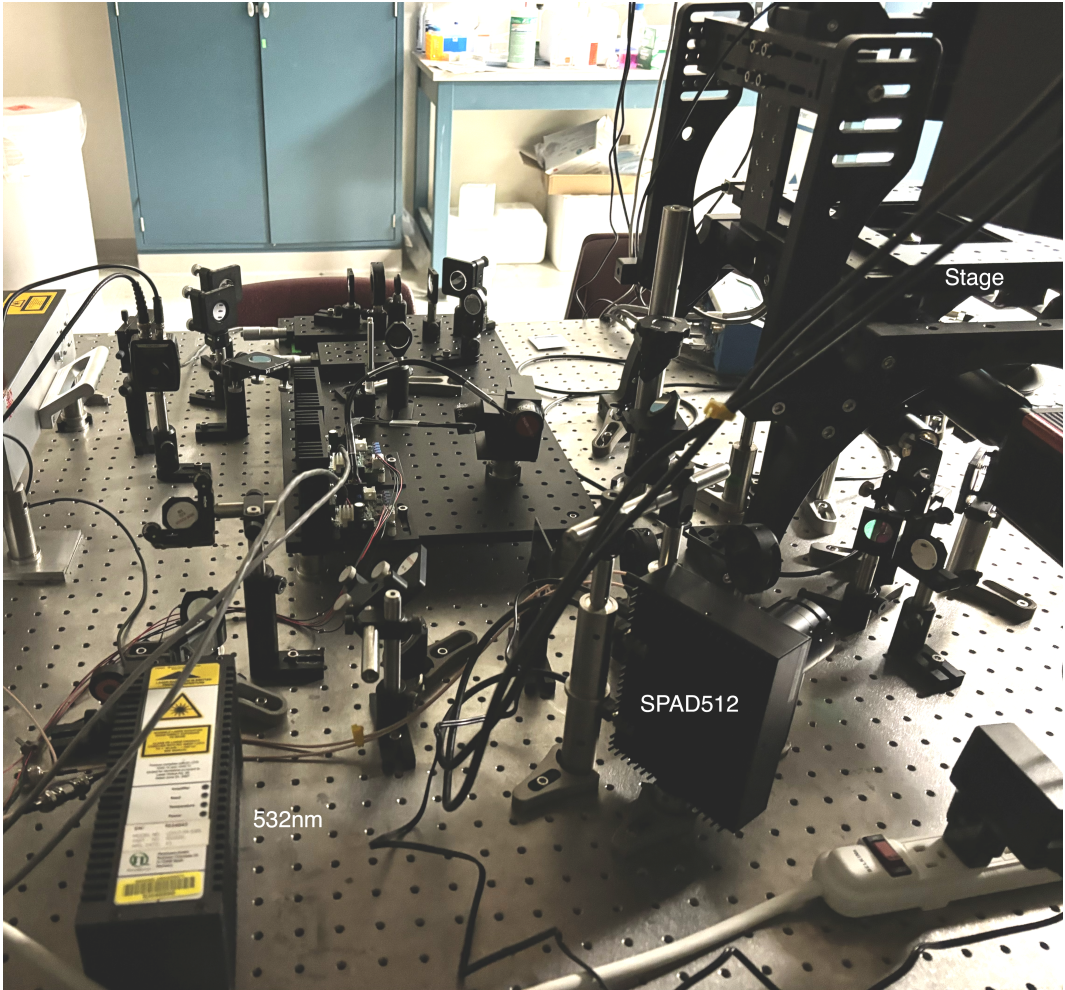


**Figure 3.2.**

tions within a pixel neighborhood [8]. However, the number of fluorescent active emitters in a region of interest remains critical prerequisite information in single molecule localization.

In this study, we present a method for widefield single photon counting in order to rigorously count fluorophores in the sample and subsequently constrain single molecule localization. We investigate the theoretical properties of the zero-lag second-order coherence function  $g^{(2)}(0)$  for widefield photon counting and its spatial properties. Using Bayesian analysis, we derive a posterior distribution on the number of active fluorescent emitters in a region of interest. We then combined this with single molecule localization algorithms

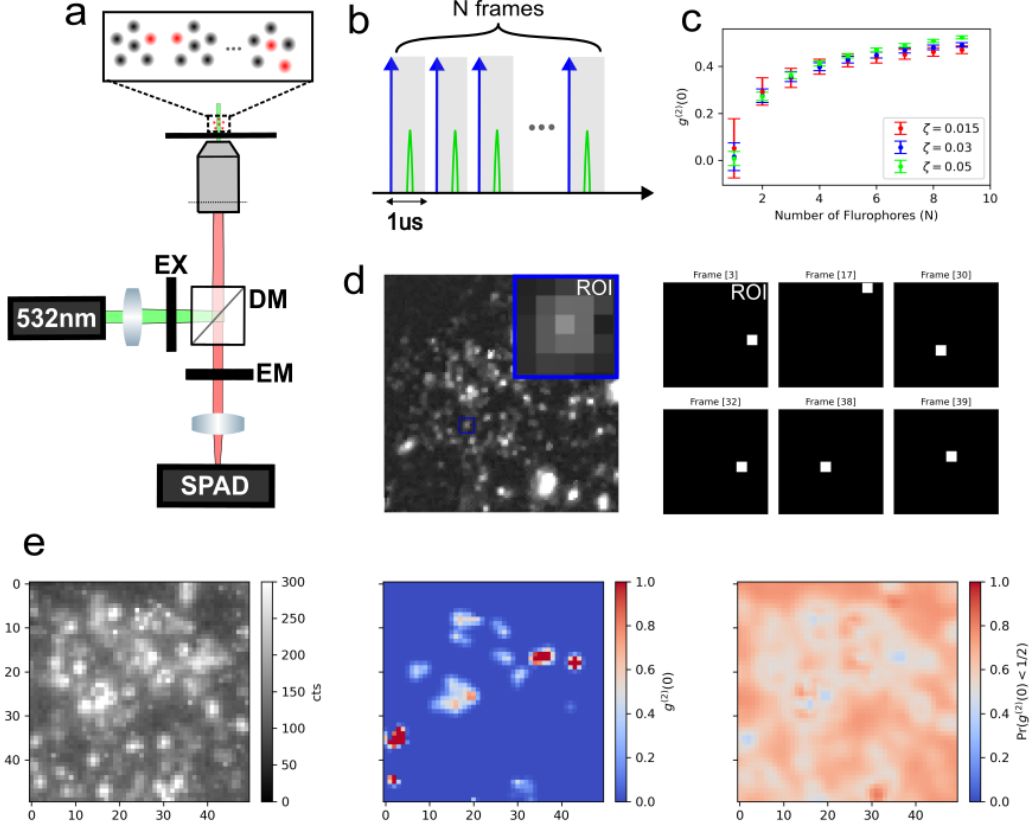


**Figure 3.3.** Single photon counting with a SPAD array (a) Conventional widefield microscopy with integrated SPAD array (b) Single photon imaging scheme using 1 $\mu$ s exposures containing a picosecond laser pulse (c) Sum of photon counts over a 5x5 region of interest (ROI), taken with  $N_{\text{frames}} = 5 \times 10^5$

and demonstrate resolution of multiple emitters using a multi-emitter fitting algorithm and report localization errors with respect to the Cramer-Rao bound.

### 3.2.2 Basic Scheme

We consider a simplified description of widefield photon counting for a single photon source in the object plane labeled by a continuous-valued coordinate  $\theta = (x_0, y_0)$ . The spatial profile  $O$  of the field in image space is presumed to have a Gaussian shape [2]–[4].

$$O(x, y) = \frac{1}{2\pi\sigma^2} e^{-\frac{(x-x_0)^2+(y-y_0)^2}{2\sigma^2}} \quad (3.1)$$

Therefore the field operator in object space is  $\hat{E} \propto \hat{a}$  and in image space  $\hat{E} \propto O(x, y)\hat{a}$ . Since our SPAD detectors at the image plane must be discrete, the total field at a detector element  $k$  centered in image space at  $s_k = (u_k, v_k)$  is then given by integrating over pixels of width  $\delta$ . Moreover, the Gaussian  $O$  is presumed to be isotropic and therefore we have  $\hat{E}(s_k) \propto \Gamma_x(u_k, x_0)\Gamma_y(v_k, y_0)$ . For example,

$$\begin{aligned}\Gamma_x(u_k, x_0) &= \\ \frac{1}{\sqrt{2}} \left( \operatorname{erf} \left( \frac{u_k + \frac{1}{2} - x_0}{\sqrt{2}\sigma} \right) - \operatorname{erf} \left( \frac{u_k - \frac{1}{2} - x_0}{\sqrt{2}\sigma} \right) \right)\end{aligned}$$

We now consider the case of pulsed excitation where the interval between pulses much longer than the fluorescence lifetime. Upon excitation of an isolated fluorescent emitter, a photon is detected at a particular detector element  $k$  with probability  $\zeta_k \propto \langle \hat{E}^\dagger(s_k)\hat{E}(s_k) \rangle = \frac{1}{2}\Gamma_x^2\Gamma_y^2 \operatorname{Tr}(\rho a^\dagger a)$  where  $\rho$  is the density matrix for a two-level system. Similarly, the probability of detection in a region of interest collecting all photons emitted is  $\zeta \propto \operatorname{Tr}(\rho a^\dagger a)$ . Here, we are primarily concerned with the latter quantity, and its application in counting fluorescent emitters.

By temporarily ignoring the spatial profile described by (1), we derive a likelihood on the number of fluorophores in a small ROI with a lateral dimension  $d = 5$  pixels. For  $N$  fluorophores emitting photons which can be detected within a ROI of the SPAD array, the number of signal photons measured  $n_{\text{signal}}$  following a single excitation pulse will have Binomial statistics  $n_{\text{signal}} \sim \text{Binom}(N, \zeta)$ . Photon pile-up at a single detector element can be safely neglected in this model due to its relatively low likelihood. We then model the background signal within the region of interest as a coherent state, which must follow Poissonian statistics  $n_{\text{background}} \sim \text{Poisson}(\lambda)$  for an expected number  $\lambda$  of background counts in the ROI per frame. The total number of counts  $n = n_{\text{signal}} + n_{\text{background}}$  detected in the region of interest following a single pulse is then distributed by the likelihood

$$p(n = n' | N, \zeta) = \sum_{i=0}^{\infty} \binom{N}{i} \zeta^i (1 - \zeta)^{N-i} \frac{\lambda^{n'-i}}{(n'-i)!} e^{-\lambda} \quad (3.2)$$

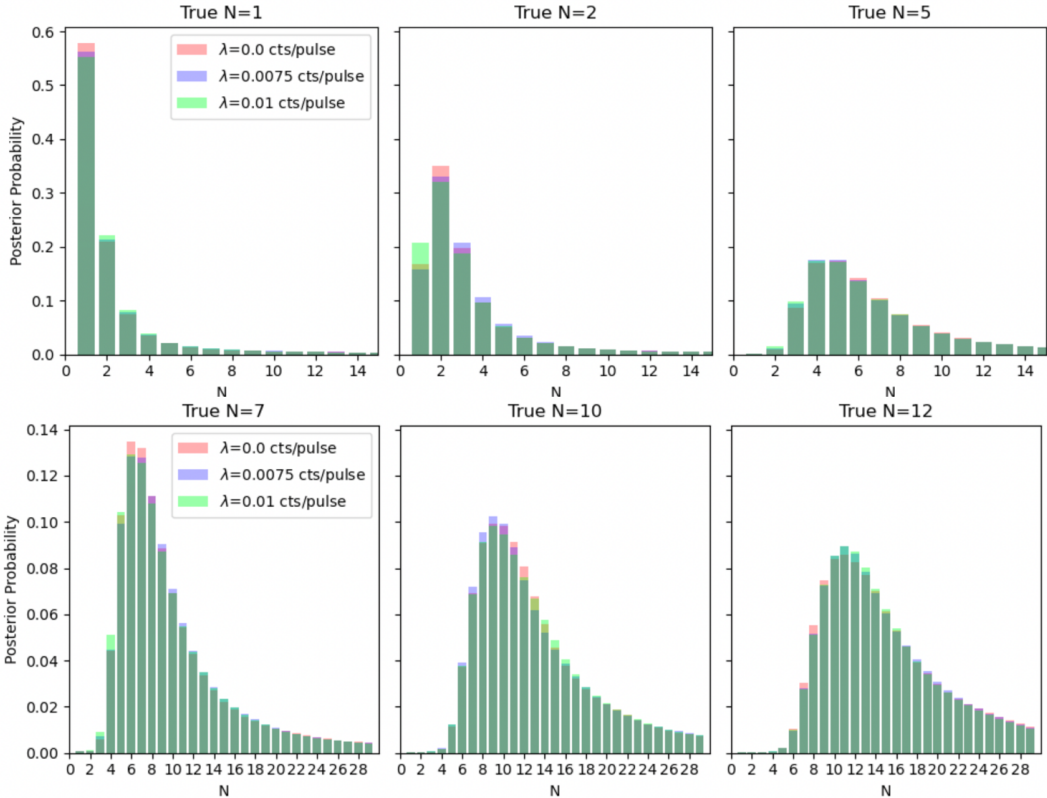


**Figure 3.4.**

The expression in (2) represents a convolution of Poisson and Binomial probability mass functions. This result is the primary means of inference of the number of active emitters  $N$  in a ROI.

In order to begin to perform localization in non-sparse ROIs, we write a posterior distribution on the Binomial parameters used in the likelihood (2) using Bayes rule

$$p(N, \zeta | x) \propto p(x|N, \zeta)p(\zeta) \quad (3.3)$$

We use a Gaussian prior on  $\zeta$  i.e.,  $p(\zeta) = \mathcal{N}(\mu_\zeta, \sigma_\zeta)$  with  $\mu_\zeta = 0.01$  and  $\sigma_\zeta = 0.005$ . Prior uncertainty in the value of  $\zeta$  stems from fluorophores with potentially heterogeneous photophysical properties as well as varying laser power throughout the excited region. This posterior can be integrated over  $\zeta$  to produce a posterior distribution on the fluorophore

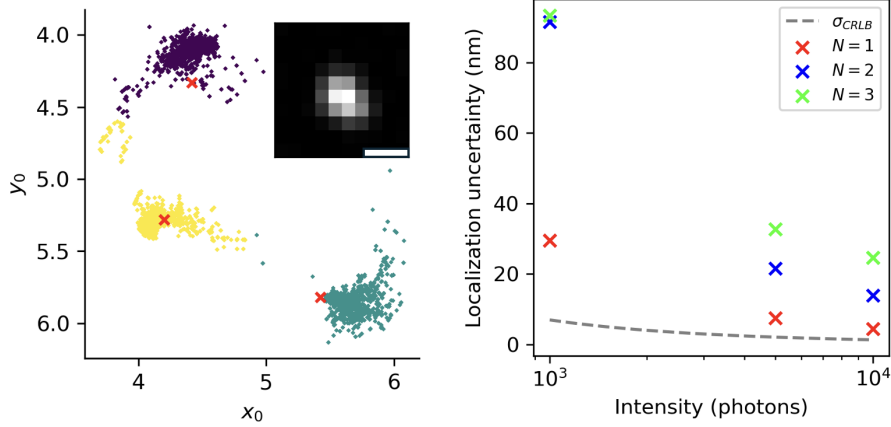


**Figure 3.5.** Single and multi-emitter localization error on sums of photon counts. (left) Localization uncertainty for simulated data for different values of  $N$ , plotted with respect to the Cramer-Rao lower bound, shown in dashed gray. (right) Multi-emitter localization by MCMC sampling for  $N = 3$ , colors indicate a cluster of samples i.e., a single localization. All data was generated with a background rate  $\langle \mathbf{n}_{\text{background}} \rangle = \lambda N_{\text{frames}} / d^2$  per pixel. Scalebar 360nm

number  $N$  i.e.,  $p(N = N'|n) \propto \int_0^1 \prod_j p(n_j|N', \zeta)p(\zeta)d\zeta$  which can be estimated using Monte Carlo methods. The final posterior is then estimated by minibatching the data into batches of  $10^3$  frames and averaging the posterior  $p(N|n)$  over minibatches. The fluorophore number  $N$  within each ROI is then estimated by the maximum a posteriori (MAP) estimate  $N^*$  given by this distribution.

For localization, we notice that (2) is well approximated by a Poisson distribution for a large frame number, making the localization procedure similar to conventional intensity-based methods [31]. Denoting the fluorophore coordinates by  $\theta$  and vector of total counts in the region of interest  $\mathbf{n}$ , we have the following log-likelihood

$$\ell(\mathbf{n}|\theta) = -\log \prod_k \frac{e^{-(\mu_k)} (\mu_k)^{\mathbf{n}_k}}{\mathbf{n}_k!} \quad (3.4)$$

$$= \sum_k \log \mathbf{n}_k! + \mu_k - \mathbf{n}_k \log (\mu_k) \quad (3.5)$$

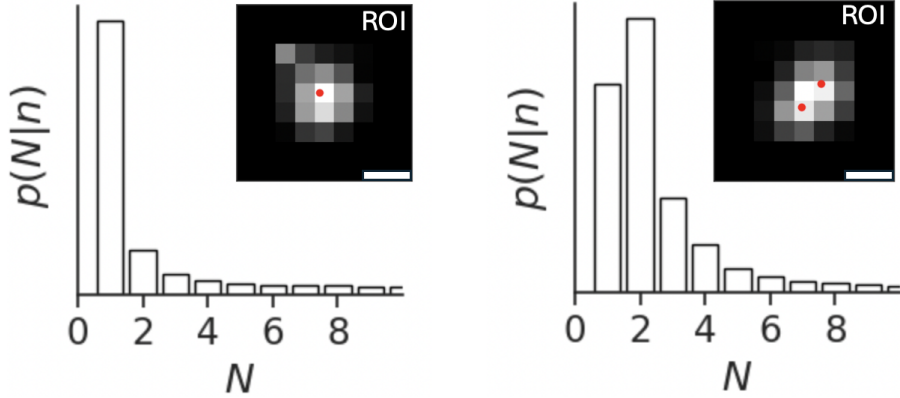


**Figure 3.6.** Posteriors on the number of fluorescent emitters  $N$  and localization for  $N^* = 1$  (left) and  $N^* = 2$  (right) quantum dots. Scalebars 360nm

where, in the multi-emitter regime the expected photon count at a pixel is  $\mu_k = \langle \mathbf{n}_k \rangle = \sum_{m=1}^{N^*} \mu_{k,m}$  given  $\mu_{k,m} = \zeta N_{\text{frames}} \Gamma_x(u_k, x_{0,m}) \Gamma_y(v_k, y_{0,m}) + \lambda N_{\text{frames}}/d^2$ . In the multi-emitter regime, optimization of (4) by sampling is a suitable choice (see Results).

### 3.2.3 Results

Quantum dots coated on a glass coverslip were excited using a picosecond 532nm pulsed laser triggered at 500kHz. Emission light was collected using an oil-immersion 100 $\times$  objective with numerical aperture (NA) 1.4 (Nikon). The emission signal was then filtered to exclude the laser line (Semrock) and projected onto the SPAD512 sensor (Pi Imaging Technologies) using a tube lens. A simplified diagram of the complete system is depicted in (Figure 1a). Each acquisition consists of  $N = 5 \times 10^5$  frames (500ms), synchronized with each laser pulse, using a 1us exposure per frame (Figure 1b,d). To confirm the presence of single photon sources in the sample, we investigated properties of the zero-lag second order coherence function  $g^{(2)}(0)$ . The following empirical estimate of  $g^{(2)}(0)$  is used [33]

$$g^{(2)}(0) = \frac{G^{(2)}(0) - B}{\langle G^{(2)}(m \neq 0) \rangle - B} \quad (3.6)$$

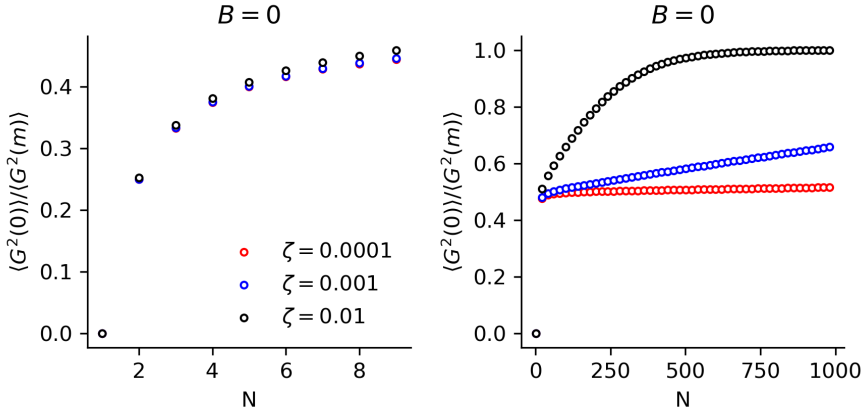


**Figure 3.7.**

where  $B = N_{\text{frames}}\lambda\zeta$  is the expected number of background-signal coincidences in the region of interest. The quantity  $G^{(2)}(m)$  represents the number of signal-signal coincidences in the region of interest at a lag time  $m$ . The quantity  $\langle G^{(2)}(m \neq 0) \rangle$  is the average number of coincidences in pairs of frames at nonzero lag  $m \in [1, 100]$ , in units of frames. As expected, simulation from the likelihood (2) shows saturation of  $g^{(2)}(0)$  with increasing values of  $N$  (Figure 1c). Moreover, bright clusters of quantum dots exhibit elevated  $g^{(2)}(0)$  values as can be seen in maps of the  $g^{(2)}(0)$  computing using sliding window over the array (Figure 1e).

For localization by optimization of (4), we use Goodman and Weare's Markov Chain Monte Carlo (MCMC) algorithm [34] to sample from the posterior on fluorophore locations. In all simulations we assume a uniform prior on coordinates over the ROI and  $\zeta$  is known and identical over fluorophores. Fluorophore locations can then be estimated from the posterior samples by K-means clustering of the  $(x, y)$  coordinates of the first particle and identification of cluster centers (Figure 2a). To validate our estimator, we compare its RMSE to the single emitter Cramer-Rao lower bound, which bounds the variance of a statistical estimator of  $\theta$ , from below (Chao 2016). For an isolated emitter, the Poisson log-likelihood (5) is convenient for computing the Fisher information matrix for  $\theta$  and thus the The Fisher information is [31]

$$I_{ij}(\theta) = \sum_k \frac{1}{\mu_k} \frac{\partial \mu_k}{\partial \theta_i} \frac{\partial \mu_k}{\partial \theta_j} \quad (3.7)$$

The Cramer-Rao bound is then found by  $\text{var}(\theta) \geq I^{-1}(\theta)$ . We find that for thousands of expected signal photon counts, localization uncertainty lies in an acceptable range for localization microscopy (Figure 2b). Example posteriors and multi-emitter fitting on experimental quantum dot data are found in (Figure 3). The  $\zeta$  value is treated as unknown but homogeneous across fluorophores in the ROI. *A major criticism is likely that we have not measured  $\zeta$  precisely and that we can only provide self-consistency for its simultaneous value with  $N$ .*

Averaging  $G^{(2)}(0)$  over many realizations (sequences of  $N_{\text{frames}}$ ), gives the expected value  $\langle G^{(2)}(0) \rangle$

$$\langle G^{(2)}(0) \rangle = N_{\text{frames}}(1 - (1 - \zeta)^n - n\zeta(1 - \zeta)^{n-1}) \quad (3.8)$$

Since  $G^{(2)}(m)$  is already averaged over  $m$ ,  $\langle G^{(2)}(m) \rangle$  is effectively a constant over realizations, and must be

$$\langle G^{(2)}(m) \rangle = N_{\text{frames}}(1 - ((1 - \zeta)^n))^2 \quad (3.9)$$

Ignoring the effect of background signal  $\langle g^{(2)}(0) \rangle = \langle G^{(2)}(0) \rangle / \langle G^{(2)}(m) \rangle$ , which rapidly approaches 1/2 as a function of  $N$ , and then saturates and very slowly approaches its maximum value of 1. This is consistent with the idea that for very large number of active fluorescent emitters, the statistics should become Poisson.

### 3.2.4 Discussion

Many fluorescent emitters exhibit random variations of brightness known as blinking. Blinking increases the observed photon-number fluctuations and could be expected to affect the value of  $g^{(2)}(0)$  or the posterior on the number of active fluorescent emitters. However, the signal photon number per frame will follow Binomial statistics even in the presence of blinking, the only consequence of which is an effective reduction of the detection probability

$\zeta$ . If the effect of censoring photons by blinking and lowering the quantum yield can be accounted for, the technique used here may be compatible with common super-resolution techniques such as stochastic optical reconstruction microscopy (STORM).

The acquisition times necessary to obtain sufficient photon counts for computing the necessary statistics can potentially be very short. Most fluorophores have relaxation times in the nanosecond range and thus photons can be collected at a rate of at tens of millions of excitation pulses per second. These rates are currently difficult to obtain, however, due to limitations in detector throughput. The SPAD camera used in this study has a minimum exposure time in the microsecond range. Furthermore, the data volume can quickly become intractable due to the need for several thousands of frames for a millisecond-scale exposure time. This is currently a complication for techniques like STORM and advancements in the automation for data acquisitions are necessary. The speed of MCMC based localization remains a limitation for post-processing, and optimization of the processing time for localization is left for future work.

In conclusion, we propose a single molecule imaging technique that allows for simultaneous counting of localization of fluorescent molecules by modeling the quantum properties of fluorescence emission. The technique does not require a nonclassical light source and is designed to supplement standard single molecule localization microscopy techniques. The proposed method can be implemented with a standard widefield fluorescence microscope.

## 4. Fluorescence nanoscopy in the study of chromatin organization

### 4.1 Background

Chromatin is a complex and dynamic structure that packages eukaryotic DNA with histones. Genomic functions such as gene expression, DNA synthesis, and DNA repair are regulated by the higher-order chromatin organization. The chromatin structure and architecture are strictly controlled and constantly remodeled as cells differentiate, divide, and respond to genomic insults (Auerbach et al., 2009; Chien and van Noort, 2009; Clapier and Cairns, 2009; Misteli, 2007; Salvador Moreno et al., 2019; Vidi et al., 2014).

While DNA linearly encodes genetic information, serving as a template for RNA and protein production, the temporal and spatial organization of chromatin plays a fundamental role in determining intranuclear activities and gene stability (Cuvier and Fierz, 2017; Dion and Gasser, 2013). On a basic level, fast (microseconds to seconds) local structural fluctuations in nucleosomes transiently expose buried DNA sites, thus providing temporary access to interaction sites (Choy and Lee, 2012). Similarly, chromatin fibers are subject to rapid conformational dynamics (Kruithof et al., 2009; Li et al., 2016; Poirier et al., 2009). This intrinsic motion of chromatin directly affects molecular interactions at the local level by dictating the accessibility of DNA for various epigenetic effectors, chromatin regulators, and transcription factors (TFs). Therefore, the nanoscale spatiotemporal profile of chromatin may modulate the interaction of DNA with regulatory molecules, impacting the global patterns of gene expression (Bintu et al., 2018; Boettiger et al., 2016; Grant et al., 2018; Xu et al., 2018).

Chromatin domains typically display stochastic motions (Marshall et al., 1997; Weber et al., 2012; Wiesmeijer et al., 2008), with rare exceptions of directional movements (Levi et al., 2005). The kinetics of chromatin are best described by sub-diffusive (or anomalous) diffusion models (Fierz and Poirier, 2019; Shukron et al., 2019).

However, the field is cluttered with apparently contradictory findings, partly due to the scarcity of suitable methods and physical models to study chromatin dynamics. Most of what we know about local chromatin motion in chromatin remodeling has been derived from ensemble measurements, which provide a population-averaged picture of biochemical access

to chromatin. Recent advances using single-molecule approaches have enabled the direct observation of the dynamics of individual molecules, allowing measurement of their respective spatiotemporal localizations and providing functional clues/implications. Particularly, time-course recording of chromatin loci movements provides quantitative measures, allowing us to assess the spatiotemporal dynamics of chromatin and deduce its biophysical properties.

#### 4.1.1 Labeling strategies of chromatin

To successfully illuminate chromatin structure and dynamics, advanced microscopy systems and single-molecule tracking algorithms must be combined with effective labeling techniques. Visualization of chromatin generally involves tagging fluorescent reporters to the central components of the eukaryotic central dogma: DNA, RNA, and proteins. Below, we review various classical and emerging chromatin labeling strategies based on proteins and DNA (summarized in Table 1).

#### 4.1.2 Chromatin-Associated Protein-Based Labeling Strategies

Core histones (H2A, H2B, H3, and H4), the fundamental units of chromatin tightly wrapped by DNA molecules, are common targets for imaging. In fixed cells, chromatin-associated proteins can be visualized through immunostaining with antibodies (Conic et al., 2018; Ricci et al., 2015; Xu, 2018). In live cells, histones can be directly fused with fluorescent proteins (FPs) (Belmont, 2001; Das et al., 2003; Kanda et al., 1998; Mora-Bermudez and Ellenberg, 2007). However, this method faces limitations in controlling labeling density, making it less quantitative for highly expressed proteins.

Photo-active fluorescent proteins (PAFPs) have been developed to address this limitation, allowing real-time quantitative characterization of protein clustering. This method can be combined with other technical strategies such as single-molecule tracking and super-resolution imaging (Cisse et al., 2013; Manley et al., 2008; Nozaki et al., 2017). For instance, the Zhuang lab engineered mMaple2 and mMaple3, which showed substantially reduced dimerization tendencies, allowing live-cell imaging for up to 5 hours without detectable phototoxicity or photobleaching (Wang et al., 2014; Baker et al., 2010). Alternatively, histone

labeling in live cells can utilize prevalent self-label tags (Liss et al., 2015; Stagge et al., 2013), such as Halo Tag, Snap Tag, CLIP tag, and TMP Tag, which offer advantages like small size, brightness, photostability, monomerization, and adjustable fluorescent dye concentration, demonstrating superior performance in single-molecule imaging (Grimm et al., 2017; Nagashima et al., 2019; Nozaki, 2017).

Other genomic elements can also be fluorescently labeled to assess structure and dynamics, including telomeres (Avogaro et al., 2018), centromeres (Avogaro and Querido, 2018; Gasser, 2002), H-NS or HU in *E. coli* (Wang et al., 2011), heterochromatin proteins (Hu et al., 2013), and transcription factors (TFs) (Elf et al., 2007; Gebhardt et al., 2013). Despite their stability and efficacy, protein-based labeling methods have drawbacks, such as being suitable only for global or non-specific investigations and the potential for labeling artifacts due to overexpressed FPs.

#### 4.1.3 DNA-Based Labeling Strategies

##### Non-sequence Specific

Several cell-permeable DNA dyes, including Hoechst (Green and Sambrook, 2017), 4,6-diamidino-2-phenylindole (DAPI), YOYO-1, and DRAQ5, strongly bind to DNA, offering simple labeling methods with excellent photostability in fixed cells. Fluorescently labeled dNTPs, which form the DNA backbone, can also demonstrate chromatin structure (Bu et al., 2019). However, these fluorescent DNA dyes generally lack specificity, which is crucial for elucidating how DNA structure affects its functional outcomes.

##### Sequence Specific

Fluorescence in situ hybridization (FISH) has been developed to detect and locate sequence-specific DNA/RNA in fixed cells using probes complementary to the target sequence (Bayani and Squire, 2004; Beliveau et al., 2015). Recent advancements in FISH, such as MerFISH, QFISH, smFISH, seqFISH, and CASFISH, have improved specificity, sensitivity, multiplexing, throughput, and qualitative analysis (Deng et al., 2015; Haimovich and Gerst, 2019;

Iourov, 2017; Moffitt and Zhuang, 2016; Shah et al., 2018; Xia et al., 2019; Zhang et al., 2018). Despite its advancements, FISH does not elucidate dynamics in living environments.

Locus-specific labeling in live cells remains in high demand. This has been achieved through either inserting artificial DNA sequences next to target genes, such as the repressor-operator array system (Lac operator (LacO) and Tet operator (TetO) systems), or modified genome-editing tools with inactive nucleases like zinc finger proteins (ZFPs), transcription activator-like effectors (TALEs), and clustered regularly interspaced short palindromic repeats (CRISPRs). The LacO-Laci-FP and TetO-TetI-FP systems are derived from the lactose and tetracycline operons of *E. coli*, respectively. Lac and Tet repressor proteins fused to FPs serve as tracking foci, recognizing repressor tandem repeat sequences inserted next to the position of interest (Ding and Hiraoka, 2017; Loiodice et al., 2014). Multiple systems and repressor segments can be used simultaneously in a single cell to enhance system multiplicity and fluorescent amplification (Backlund et al., 2014; Roukos et al., 2013; Tasan et al., 2018).

Point accumulation for imaging in nanoscale topography (PAINT) techniques are attractive for single-molecule localization microscopy due to their lack of restriction by photon budget. First demonstrated by Jungmann et al. in 2010 (Jungmann et al., 2016), DNA-based PAINT has been explored and improved over the past decade. Quantitative PAINT (qPAINT), Förster resonance energy transfer PAINT (FRET-PAINT) (Jungmann et al., 2016), and Exchange PAINT have been developed to generalize the use of DNA origami to reveal cellular interactions, although off-target challenges remain (Nieves et al., 2018). Additionally, the ParB-INT system can similarly insert a 1 kb INT element, providing a strong signal without interfering with chromatin dynamics and transcription (Saad et al., 2014). Nonetheless, any intrusive DNA insertion can potentially perturb function and alter chromatin locus position and mobility. Non-intrusive methods such as ZFPs, TALEs, and CRISPR-dCas9 avoid these constraints, operating without artificial DNA insertion (Chen et al., 2016; Lindhout et al., 2007; Ma et al., 2013). These systems rely on modular proteins with specific DNA recognition, where endonuclease-deficient proteins are usually fused with FPs as detectable signals. Among these strategies, CRISPR imaging systems are gaining attention. Chen et al. re-engineered the type II system to visualize both repetitive ele-

ments in telomeres and non-repetitive MUC4 (Chen et al., 2013). For multicolor imaging within the CRISPR system, one strategy is to use fluorescent Cas9 orthologs from different bacterial species simultaneously, such as *Streptococcus pyogenes* (SpCas9), *Neisseria meningitidis* (NmCas9), and *Streptococcus thermophilus* (St1Cas9) (Ma et al., 2015). Another alternative strategy involves engineering sgRNA into a scaffold RNA (scRNA) to encode information about the gene of interest and multiple fluorescent reporters (Zalatan et al., 2015). Recent modifications to CRISPR imaging systems, such as CRISPR-display (Shechner et al., 2015) and CRISPR-rainbow (Ma et al., 2016), suggest promising applications for investigating chromatin organization and visualizing genome instability and rearrangement (Chen and Guan, 2016).

#### 4.1.4 Instrumentation for Intranucleus Imaging

Among many factors that determine the accuracy of chromatin loci movement, spatial resolution is the parameter that dominates the reliability of downstream biophysical analysis (Burov et al., 2013). Therefore, for most reported work in intranucleus chromatin imaging, objectives with high numerical aperture (N.A. > 1.2) are employed. As indicated in the previous section, multiple fluorophores are used in chromosome labeling strategies to ensure adequate fluorescent signal; consequently, there are few limitations on imaging modalities, and various microscopes can be used for chromatin imaging.

For many intranucleus imaging experiments, an epi-illumination fluorescent microscope equipped with a modern camera (EMCCD or sCMOS) (Figure 1A) can provide time-course recording of live cells. Additionally, emerging LED light sources are replacing laser excitation in these microscopes, which significantly reduces the cost of the microscope (Albeau et al., 2008; Hattori et al., 2009; Zheng, 2013). Another widely applicable imaging system for chromatin imaging is the confocal microscope (Figure 1B), which offers good z-sectioning capability to reduce out-of-focus background. However, the applicability of confocal microscopy for chromatin motion is due to the relatively slow motion in the nucleus ( $D < 0.001 \text{ m}^2/\text{s}$ ) (Shukron et al., 2019). Despite its advantages, confocal microscopy suffers from

intrinsic limitations such as photo-bleaching/photo-toxicity and poor temporal resolution, which restrict their applications for sensitive chromatin imaging at the single-molecule level.

The usual alternative to epi-illumination microscopes is total internal reflection fluorescence microscopy (TIRF) (Figure 1C), which can capture photons from a single fluorescent molecule. However, it is not suitable for chromatin imaging in the nucleus due to its poor penetration depth ( 200 nm).

Emerging light sheet illumination offers solutions to the aforementioned challenges and achieves a balance among spatiotemporal resolution, photo-bleaching effects, and background reduction (Figure 1E). In 2008, a simple yet efficient light sheet illumination method was proposed to generate a highly inclined and laminated optical sheet (HILO) for single-molecule imaging (Tokunaga et al., 2008). The high spatial resolution can be retained thanks to the high N.A. objective, and HILO illumination significantly reduces total illumination doses on the cell, though it results in a largely reduced field of view (Figure 1D). Since then, light sheet illumination has garnered tremendous attention for its advantages in reducing phototoxicity, enhancing sectioning capability, and enabling live-cell three-dimensional (3D) imaging. Early development of light sheet microscopy, using two orthogonal objectives (N.A. 0.65) for excitation and/or emission, has shown great performance for 3D imaging of tissues, embryos, and organs (Keller et al., 2015; Keller et al., 2010; Keller et al., 2008; Tomer et al., 2011). However, its application in single-cell and even single-molecule imaging was limited by geometric hindrance when using two high N.A. objectives. Recent efforts have focused on developing new light sheet modalities for single-cell 3D imaging. An AFM cantilever was initially used to reflect the illumination light sheet by 90 degrees to bypass geometric hindrance (Gebhardt, 2013). A similar idea was proposed using a microfabricated reflecting chip next to the sample reservoir (Galland et al., 2015). Both approaches can generate a thin sheet of light with a beam waist of 1 m. Furthermore, the lattice light sheet (LLS) microscope, which generates the light sheet with a Bessel beam, significantly reduces the thickness of the light sheet to 300 nm (Chen et al., 2014). The LLS has demonstrated superior performance in terms of spatial resolution, temporal resolution, phototoxicity, and sensitivity (Gao et al., 2019). However, generating optical lattices requires a complex, expensive, and lossy optical train. A recent study proposed a simple and universal optical process, described

by a mathematical theorem as field synthesis, to create any type of light sheet, including the lattice light sheet (Chang et al., 2019). This approach can be integrated with any light sheet imaging system to enable lattice light sheet imaging.

The further development of imaging modalities for chromatin imaging will aim at a light sheet imaging technique that balances various imaging parameters and provides time-course recording of chromatin motion in 3D. Generally, chromatin can be modeled as beads on a string. To determine polymer models that accurately reflect the behavior of chromatin inside the nucleus, one must compare extracted physical parameters from real experimental chromatin data with those predicted from the model. However, physical models often fail to infer actual chromatin dynamics due to inconsistencies between modeling and experiments. This discrepancy arises because 2D imaging data cannot offer positional information of chromatin motion in 3D, whereas physical modeling is in 3D. A recent study by the Misteli group compared 2D and 3D distance measurements in the cell nucleus (Finn et al., 2017). While 2D measurements (i.e., positions or trajectories projected in a single plane) are practical and generally well-suited for flat nuclei in monolayer cell cultures, 3D measurements are necessary to improve accuracy, particularly for round nuclei (e.g., in 3D cultures) where the relationship between 2D and 3D distances deteriorates, and for short distances (<5 m) where the average 2D/3D discrepancy is 30 percent (Finn et al., 2017). Moreover, nuclear inhomogeneity in all 3 dimensions must be considered. For motion measurements, the 2D/3D discrepancy of 30 percent might not be very significant, but considering local fluctuations of 50 nm, the 3D nature cannot be ignored.

It is worth noting that the imaging instrumentation and analysis methods discussed here share many similarities with localization-based super-resolution microscopes, such as Fluorescence Photoactivation Localization Microscopy (PALM or fPALM) and Stochastic Optical Reconstruction Microscopy (STORM). Advances in super-resolution imaging will also benefit intranuclear chromatin imaging. For example, aspheric optics were initially utilized in super-resolution imaging to convert the z-axis position of a single molecule into a distorted point spread function (PSF) on the x-y plane using a cylindrical lens (Huang et al., 2008). This method was further developed in single-molecule imaging/tracking to register the 3D position of a moving molecule through a rotational PSF (Greengard et al., 2006; Pavani et

al., 2009; Badieirostami et al., 2010; Thompson et al., 2010). Additionally, applying super-resolution imaging to live-cell single-molecule imaging produces high-density trajectories of molecules, enabling the integration of biophysical analysis such as stochastic models of nonequilibrium motions to recover forces, subcellular organizations, diffusion kinetics, and other biophysical features at unprecedented spatiotemporal resolution (Hoze et al., 2012; Holcman et al., 2015; Hoze, 2015).

Recent progress in quantitative super-resolution imaging, such as qPAINT (Jungmann et al., 2016; Culley et al., 2018; Mockl et al., 2019), is expected to be the next booster for live-cell chromatin imaging.

#### 4.1.5 Trajectory linking

A diverse set of particle tracking algorithms utilize probabilistic models of particle motion in order to add detected particles to existing tracks. Perhaps the most fundamental particle tracking method in this category is the nearest neighbor (NN) linking algorithm first introduced by Crocker and Grier. The algorithm constructs particle trajectories by assuming that the ensemble consists of non-interacting indistinguishable particles undergoing Brownian motion. As a result, the displacement of each particle follows a Gaussian distribution, parameterized by the diffusion coefficient and the time-resolution of the sequence. The most probable assignment of detected particles to existing tracks can then be found by maximizing the product of several Gaussian distributions (Crocker and Grier, 1996). An attractive feature of this algorithm is that it is relatively simple to implement; however, assumptions that underlie the method impose limitations. In particular, if a typical displacement in one time step is comparable to the typical inter-particle spacing, tracking becomes highly error prone (Crocker and Grier, 1996). In other words, when particles are simultaneously densely distributed and undergoing fast diffusion the algorithm can fail to build accurate trajectories due to the ambiguity introduced by overlapping trajectories. This also applies to the limit of low frame rates when small displacements are not recorded by the sensor. Importantly, the method alone cannot handle cases where particles disappear permanently,

temporarily disappear due to blinking, photo-bleaching, or missed localization (Sbalzarini and Koumoutsakos, 2005)

#### 4.1.6 Quantitative Analysis of Particle Motion

Based on trajectory data, quantitative information regarding the motion of the particle can be extracted (Figure 2D). It is important to note that the chromatin structure is highly complex and cannot be exactly represented by the diffusion of individual particles. However, by treating each fluorescent foci as a point mapped in space and time, we can determine whether the motion is constrained (sub-diffusion), super diffusion, or follows normal diffusion. Thus, by using only position data (via particle tracking algorithms) and frame rate, we can uncover the following parameters.

The most common method to analyze single particle trajectories is to calculate the mean square displacement (MSD), which represents the scaling of the average squared displacement from the origin as a function of time:

$$\text{MSD} = \frac{1}{N} \sum_{i=1}^N [\mathbf{r}(t + \tau) - \mathbf{r}(t)]^2 \quad (4.1)$$

The sampling time given by  $\tau$  is interpreted as the frame rate of the camera. Certain studies have shown that the observed motion varies with different values of  $\tau$  (Amitai et al., 2017; Shukron & Holcman, 2017a). Once the MSD curve is established, the effective diffusion coefficient  $D$  and the anomalous exponent  $\alpha$  values can be obtained by curve-fitting techniques using:

$$\text{MSD}(\tau) = 2mD\tau^\alpha \quad (4.2)$$

where  $m$  is the number of dimensions. These parameters reflect the velocity of diffusion and the degree of confinement of individual particles, respectively. Importantly, different parameter values allow for further interpretation and classification of different diffusion modes of particles (Wasim & Treanor, 2018; Zhong & Wang, 2020).

By comparing the  $D$  values of all particles within the nucleus, spatial heterogeneity can be clarified. Meanwhile, different  $\alpha$  values can be fitted to different diffusion models. For

trajectories with  $\alpha = 1$ , the motion is considered to be Brownian motion; when  $\alpha > 1$ , it is said to be directed motion; and  $\alpha < 1$  is classified as confined (or immobilized) diffusion.

While the calculation of  $D$  and  $\alpha$  is particularly reliant on the length of the trajectory and the number of data points, recent investigations have built diffusion color maps of fluorescently labeled histones by computing vast amounts of super-resolution trajectories. This approach aims to reveal mechanisms or interactions in cell biology (Amitai & Seeber, 2017; Barth et al., 2020; Nozaki & Imai, 2017).

#### 4.1.7 Polymer Models for Chromatin Dynamics

It is well-known that the DNA double helix structure consists of millions of base pairs chained together by the sugar-phosphate backbone. DNA, being a molecule built from many similar monomers bonded together, is naturally analyzed using a polymer model. The simplest polymer model for chromatin is the Rouse polymer model, which discretizes it into monomers connected by springs, resembling the string-of-beads structure observed under the electron microscope. Various forces acting on chromatin result in constrained dynamics, leading to significant variability in the anomalous exponent  $\alpha$  for the dynamics of a chromatin locus.

To refine the modeling of chromatin properties according to the exponent  $\alpha$ , the  $\beta$ -polymer model was introduced. This model accounts for mid-range and long-range interactions between monomers, not just those between the nearest neighbors as in the Rouse polymer model. In this model,  $\alpha$  shows a decay curve with distance along the chain. While  $\alpha = 0.5$  in the traditional Rouse polymer model, the  $\beta$ -polymer model can be selected to address cases where  $\alpha$  is in the range of 0 to 0.5 (Amitai & Holcman, 2013; Amitai & Seeber, 2017; Hajjouli et al., 2013). Thus, local interactions between monomers can be inferred from the anomalous diffusion exponent using this construction.

Furthermore, as the polymer model usually folds at different spatial scales and generates various sizes of loops, a simulation model adding connectors between randomly chosen non-nearest neighbor monomer pairs, known as the randomly cross-linked (RCL) polymer model, was presented. In this model,  $\alpha$  is reduced to below 0.5 by adding connectors. Recent

evidence suggests that the number and distribution of connectors impact physical parameters in various ways, but this domain remains underexplored (Shukron & Holcman, 2017a, b). Notably, the RCL polymer model may be crucial for studying dynamics in processes such as CTCF and cohesion regulating chromatin loop stability (Hansen et al., 2017). Additionally, sub-diffusion with an exponent  $\alpha > 0.5$  can occur in some polymer models, potentially involving different types of forces such as deterministic forces, directed motion, or other monomer interactions (self-avoiding and bending interactions).

#### 4.1.8 Super resolution of chromatin nanodomains

The interplay between chromatin structure and phase-separating proteins is an emerging topic in cell biology with implications for understanding disease states. Here, we investigate the functional relationship between bromodomain protein 4 (BRD4) and chromatin architecture. By combining molecular dynamics simulations with live-cell imaging, we demonstrate that BRD4, when phosphorylated at specific N-terminus sites, significantly impacts nucleosome nanodomain (NN) organization and dynamics. Our findings reveal that enhanced chromatin binding activity of BRD4 condenses NNs, while both loss or gain of BRD4 chromatin binding reduced diffusion of single nucleosomes, suggesting a role for BRD4 in the regulation of nanoscale chromatin architecture and the chromatin microenvironment. These observations shed light on the nuanced regulation of chromatin structure by BRD4, offering insights into its role in maintaining the nuclear architecture and transcriptional activity.

## 4.2 Introduction

The cell nucleus is a densely packed environment with chromatin comprising a dominant component. The compartmentalization of chromatin with other intranuclear components by phase separation is therefore an efficient strategy to ensure precise spatial and temporal coordination of complex dynamics. A growing number of phase separated nuclear bodies have been identified, including transcriptional condensates [35], [36], nuclear speckles [37], and DNA damage repair foci [38]; however, the interplay of phase separated condensates with the underlying chromatin structure remains poorly understood. Transcriptional con-

densates have been identified as an ideal model to study the kinetic and thermodynamic contributions of chromatin substrate binding, as the ability of transcriptional activators to both condense and bind chromatin is well established [35], [39]–[42]. Here, we extend this effort by investigating the regulation of chromatin structure by phase separated transcriptional condensates. We focus on the BRD4 protein - a well-studied transcriptional activator that localizes to acetylated chromatin sites [43], recruits pTEF-b, and initiates transcription of key genes involved in signal response, immunity, and oncogenesis [44].

The BRD4 long isoform is characterized by structured N-terminal tandem acetyl-lysine binding bromodomains and an extra-terminal domain, connected by intrinsically disordered regions [45]. Perhaps the most fundamental of BRD4 functions is the ability to bind to acetylated chromatin through bromodomain 1 (BD1) and bromodomain 2 (BD2) that are in tandem within the N-terminal part of the protein. BRD4 inhibitors such as (+)-JQ1 competitively bind to the acetyl-binding pocket of BRD4, displacing BRD4 from chromatin [46]. It is also well known that BRD4 association with acetylated chromatin is enhanced by casein kinase II (CK2)-mediated phosphorylation of seven N-terminus phosphorylation sites (NPS), followed by intramolecular rearrangement of BRD4 protein and/or BRD4 dimerization [47], [48].

Recent studies have demonstrated that BRD4 is present in discrete nuclear bodies that occur at super-enhancers, which exhibit properties of other well-studied biomolecular condensates, including rapid recovery of fluorescence after photobleaching and sensitivity to 1,6-hexanediol, which disrupts liquid-like condensates [35]. Both BRD4 long and short isoform are found in phase separated condensates in the nucleus and are associated with active gene transcription1. Importantly, CK2-mediated NPS phosphorylation state regulates chromatin binding activity of BRD413 as well as BRD4 phase separation [45]. This has led to the conclusion that phosphorylation of BRD4 inhibits interaction with chromatin and reduces phase separation, while remaining necessary for active gene transcription. Moreover, phosphorylated and unphosphorylated BRD4 form different molecular associations transient polyvalent associations of unphosphorylated BRD4 contrast with the stable dimeric interaction and chromatin binding of phosphorylated BRD4 [48]. We therefore speculated

that BRD4 chromatin binding may be necessary for maintaining NN structure and single nucleosome dynamics.

## 4.3 Results

### 4.3.1 Colocalization of BRD4 mutants with nucleosome nanodomains

To address the role of BRD4 binding and phase separation on chromatin structure, we express FLAG-tagged BRD4 mutants with NPS or bromodomain mutations in HeLa cells and measure their effects on chromatin organization. In particular, we express a constitutively phosphorylated (7D mutant), constitutively unphosphorylated (7A mutant), and bromodomain-deactivated (BD mutant) protein (Figure 1a,b). Colocalization analysis of FLAG-tagged 7A/7D BRD4 mutants with NNs using nearest neighbor distance distribution function  $G(r)$  showed an obvious colocalization of these mutants with NNs with respect to complete spatial randomness.

### 4.3.2 Chromatin structure and dynamics

To assess the functional role of BRD4 in maintaining the NN environment, we interrogated the dynamics of NNs, as well as their structure, in the presence of BRD4 mutants. Histone H2B was tagged with HaloTag [49] (H2B-Halo), to which a fluorescent ligand JaneliaFluor646 (JF646) can bind specifically in a living cell. Low concentrations of JF646 were used to obtain sparse labeling of nucleosomes for single-nucleosome imaging (Figure 2a,b). JF646-labeled nucleosomes in Hela cells were recorded at 10fps (200 frames, 20 s total) and a reduced diffusion coefficient was measured in cells expressing 7A, 7D, and BD mutants, with respect to cells expressing the wild-type BRD4 protein (Figure 2c,d). We then conducted super resolution imaging of nucleosome nanodomains using direct stochastic optical reconstruction microscopy (dSTORM) by promoting JF646 fluorescence intermittency with a cysteamine buffer (Figure 3a,c). JF646 is known to exhibit a transient fluorescent state lasting tens to hundreds of milliseconds and stable dark state lasting hundreds of milliseconds to seconds [50]. Two color imaging of H2B-Halo-JF646 and GFP-tagged BRD4 shows that BRD4 and NNs form complementary biomolecular condensates in the nucleus, consis-

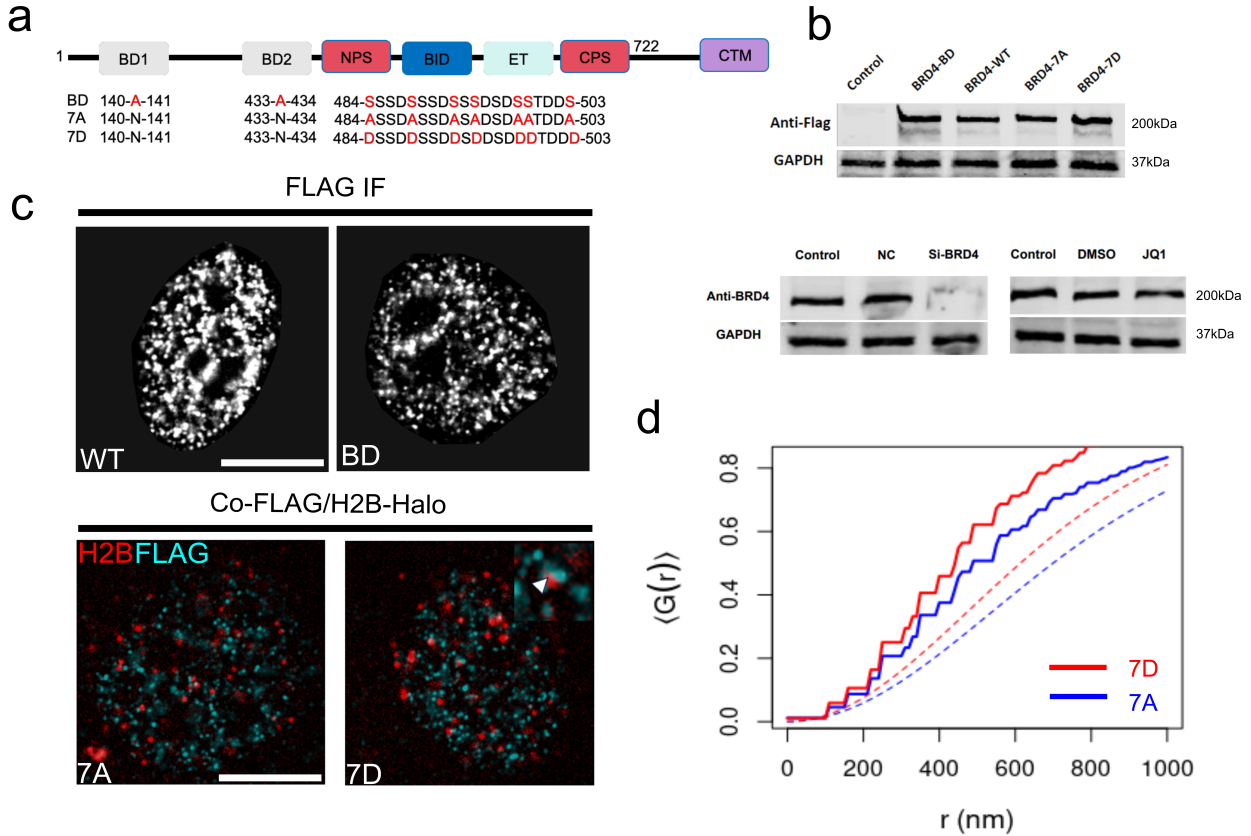


**Figure 4.1.**

tent with current models of BRD4 chromatin reading mechanism (Figure 3b). Ensemble averages of Besags L-function showed an increase in NN compaction in cells expressing the 7D BRD4 mutants, while all other groups were consistently indistinguishable from WT cells (Figure 3d).

#### 4.3.3 Heteropolymer model

To interpret our experimental findings, we adopt a heteropolymer chromatin model to capture the interaction of chromatin with multivalent BRD4-like binders (Figure 4a). The heteropolymer consists of a coarse-grained bead-and-spring chain composed of  $N_b = 200$  beads, connected by harmonic bonds with equilibrium length  $r_0$  whose energy is dened as

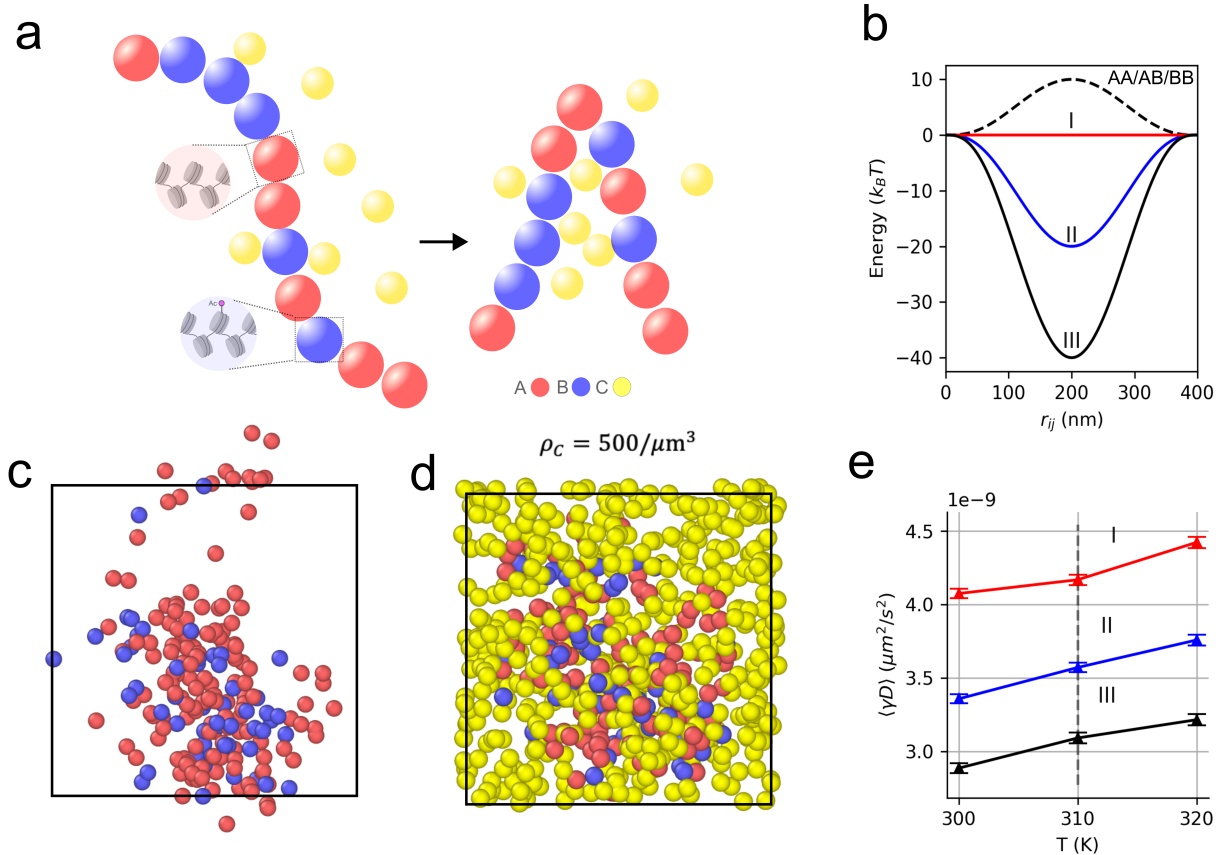


**Figure 4.2.**

$$U_{AB}(r_{ij}) = \frac{\kappa}{2}(|r_{ij}| - r_0)^2$$

where  $r_{ij}$  is a vector connecting the center of a bead of type i to a bead of type j and  $i, j \in (A, B)$ . In all simulations, we assume  $\kappa = 90k_B T r_0^2$  where  $k_B$  is Boltzmanns constant and  $r_0 = 200\text{nm}$ . Random beads in the chain are selected to represent locally unacetylated (A-type particles) and acetylated chromatin (B-type particles). B-type particles undergo multivalent interactions with a third group of C-type particles, which can promote cross-linking of the polymer. We presume a Bernoulli probably of  $p = 0.3$  for any given bead to be in an acetylated-like state. Interaction of multivalent chromatin binders with chromatin beads are then mediated by the following potential:

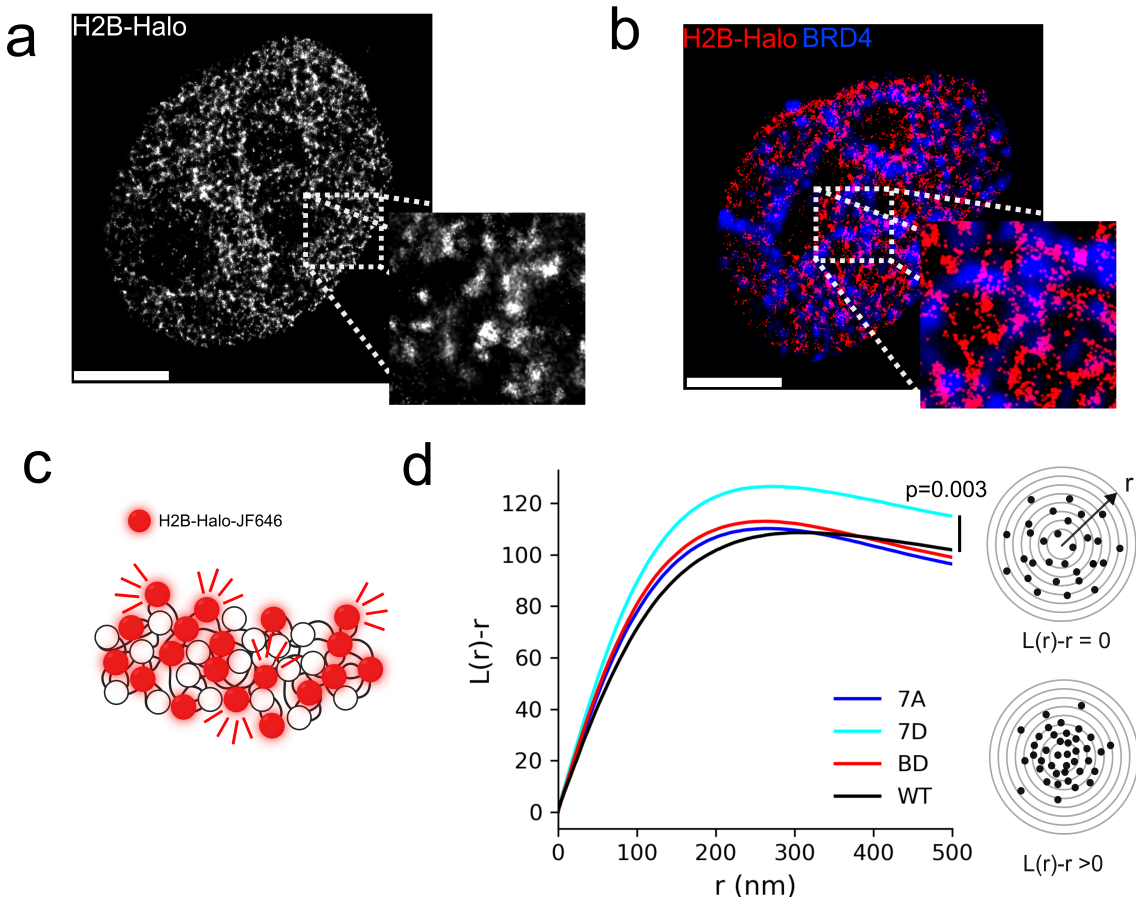


**Figure 4.3.**

$$U_{BC}(r_{ij}) = \epsilon \left( 1 - \left( \frac{|r_{ij}|}{R_0} \right)^2 \right)^3$$

where  $R_0 = 200\text{nm}$ . The potential  $U_{BC}$  is considered over a domain  $0 \leq |r_{ij}| \leq 2R_0$ . In all simulations, ten replicates were run for each condition tested. A and B type particles within the chromatin polymer have repulsive interactions with  $\epsilon = +10k_B T$ . Binding energy of the acetylated beads with binders was varied with  $\epsilon_I = 0k_B T$ ,  $\epsilon_{II} = -20k_B T$ ,  $\epsilon_{III} = -40k_B T$  (Figure 4b). The dynamics of chromatin chains are approximated by Brownian dynamics within a cubic box with side length of 10um and periodic boundary conditions. Brownian dynamics follows the stochastic differential equation.

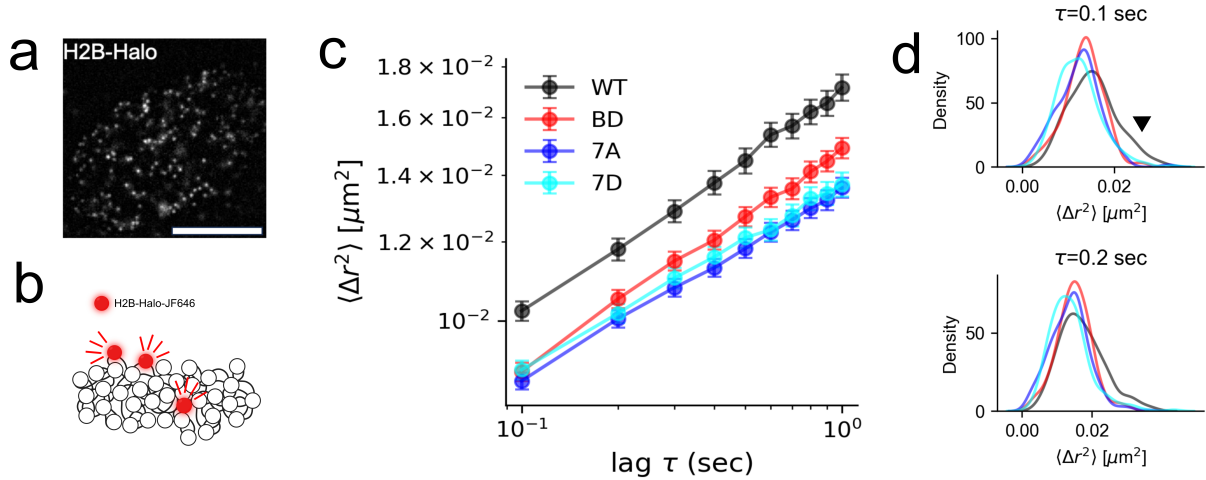


**Figure 4.4.**

$$\dot{\mathbf{r}} = \gamma^{-1} \nabla U(\mathbf{r}) + \sqrt{2k_B T} \gamma^{-1/2} \xi(t)$$

where  $\gamma$  is a diagonal friction tensor and  $\xi(t)$  is a three-dimensional delta-correlated white noise  $\langle \xi(t) \xi(t + \tau) \rangle = \delta(t, t + \tau)$ . Integrating the Brownian dynamics showed an overall reduction of the variance of the diffusion coefficient  $D$  of single beads, and linear scaling of the diffusion coefficient with respect to temperature (Figure 4e).

#### 4.4 Discussion

Our data support the model that phosphorylated and unphosphorylated BRD4 form different molecular associations in the nucleus. BRD4 nuclear localization is only weakly affected by bromodomain inhibition with monovalent BET inhibitors, while exposure to phase separation inhibitors such as 1,6 Hexanediol have a significant effect on BRD4 localization in the nucleus<sup>11</sup>. Therefore, nascent BRD4 condensates are likely seeded by unphosphorylated BRD4, followed by CK2-mediated phosphorylation, promoting chromatin interactions mediated by phosphorylated form. The stable dimeric interaction and binding of phosphorylated BRD4 to acetylated chromatin would then mediate control of the chromatin architecture by promoting cross-linking of the chromatin fiber and acting a molecular bridge between

transcriptional condensates with chromatin. Concurrently, reduced diffusivity of single nucleosomes with no overall change in NN compaction (cross-linking) in the unphosphorylated mutant is a natural result of molecular crowding resulting from overexpression of a constitutively phase separating protein, capable of multivalent interactions.

## 4.5 Materials and Methods

### 4.5.1 Cell lines, cell culture conditions, and transfection

Hela cells were cultured in DMEM supplemented with 10 percent fetal bovine serum (Gibco) at 37C 5 percent CO<sub>2</sub> in a humidified incubator. Cultures were tested routinely for mycoplasma contamination; all tests were negative. For super-resolution experiments, cells were seeded in a 35mm FluoroDish (WPI), and transiently transfected using Lipofectamine 3000 with pBREBACK-H2BHalo plasmid (Addgene plasmid 91564) (ThermoFisher), pcDNA5-Flag-BRD4-7A (Addgene Plasmid 90006), pcDNA5-Flag-BRD4-7D (Addgene Plasmid 90007), pCDNA5-Flag-BRD4-BD (Addgene Plasmid 90005), pcDNA5-Flag-BRD4-WT (Addgene Plasmid 90331)

### 4.5.2 Super-resolution imaging of nucleosome nanodomains in living cells

After transient transfection, H2B-Halotag Hela cells were incubated with 3pM JF646 HaloTag ligand overnight. Cells were imaged in a dSTORM photoswitching buffer containing 100mM MEA, 50 ug/ml Glucose Oxidase, and 3.4 mg/ml Catalase (Sigma). Buffer pH was adjusted to 8 using HCl. Movies were collected using a custom Olympus IX83 microscope body equipped with an Olympus 60X 1.25NA oil-immersion objective. During imaging cells were maintained at 37C and 5 percent CO<sub>2</sub> in a stage top incubator (Tokai Hit). Images were projected onto an ORCA-Fusion sCMOS camera (Hamamatsu) and 2000 frames were captured at 100fps. The microscope was controlled using Micromanager software. HaloTag-JF646 molecules were imaged using oblique illumination with a 640nm laser (Excelitas) held at 20mW, as measured at the back focal plane of the objective. Super resolution reconstructions were obtained using the ThunderSTORM ImageJ plugin. Background signal was subtracted using a rolling ball filter with radius of 10 pixels. Spots were fit using an

integrated Gaussian point spread function model with maximum likelihood estimation [5], [31]. Experimental conditions for single molecule tracking are nearly identical. However, H2B-Halotag HeLa cells were incubated with 3pM JF646 HaloTag ligand. HaloTag-JF646 molecules were illuminated at 10mW, 100 frames were captured at 10fps.

$$K(r) = \frac{a}{n(n-1)} \sum_{ij} I(d_{ij} \leq r) L(r) \sqrt{\frac{K(r)}{\pi}}$$

Precise x,y positions of the fluorophores are obtained, Besags L-function  $L(r)$  is used to analyze the clustering. The L-function is the following transformation of Ripley's K-function  $K(r)$

where  $a$  is the area of the window,  $r$  is the distance between,  $n$  is the number of data points and the sum is taken over all pairs of fit coordinates as shown in equation XXX. The indicator function is given by  $I(d_{ij} \leq r)$  and equals 1 if the distance is less than or equal to  $r$ . To measure degree of clustering, we use  $L(r) - r$ , which measures the deviation of a point pattern from complete spatial randomness (CSR).

#### 4.5.3 Colocalization of BRD4 mutants with nucleosome nanodomains

We colocalize FLAG-tagged 7A/7D BRD4 mutants with nucleosome nanodomains by simultaneous FLAG immunofluorescence with imaging of sparsely labeled of H2B-JF646. Puncta were detected in both channels using the Laplacian of Gaussian (LoG) detection algorithm to generate a multi-type point pattern. We then computed the nearest neighbor distance distribution function  $G(r)$ , which is the cumulative distribution function of the distance from a random H2B-JF646 puncta to the nearest BRD4-FLAG puncta. This function was computed for each cell, and then averaged over  $N = 20$  cells for each mutant to obtain  $G(r)$ . The averaged value is reported alongside the theoretical  $G(r)$  under complete spatial randomness

$$G(r) = 1 - e^{-\lambda\pi r^2}$$

Where  $\lambda$  is the expected number of points per unit area.

#### 4.5.4 Single molecule tracking

Nucleosomes were localized using an integrated Gaussian point spread function model with maximum likelihood estimation [5], [31] and tracked using TrackPy Python software. Trajectories lasting less than 80 frames were removed from further analysis. The individual mean squared displacement (MSD) is computed as  $\langle \Delta r^2 \rangle = \frac{1}{|S_\tau|} \sum_{\Delta r \in S_\tau} (\Delta r)^2$  where  $S_\tau$  is the set of all displacements in a time interval  $\tau$ . The diffusion coefficient for both simulations as well as experimental data was computed by linear regression of the formula  $\log \langle \Delta r^2 \rangle = \log 4D + \alpha \log \tau$

#### 4.5.5 Immunofluorescence

Cells grown in 35mm dishes were fixed with Formaldehyde in 1xPBS at 37C incubator for 20 minutes, and then permeabilized with 0.3 percent (v/v) Triton-X100 (Sigma-Aldrich) in PBS and blocked for 1h in 5 percent (w/v) nonfat dry milk at 4C. Cells were incubated overnight at 4C using primary antibodies anti-FLAG (Cell Signaling, clone XXX; 1:1000), and anti-BRD4 (Cell Signaling, clone E2A7X; 1:1000) in blocker. Secondary antibodies for BRD4 (Cell Signaling Anti-Mouse IgG-Alexa488, 1:1000) were used.

#### 4.5.6 Immunoblotting

Cells were washed and lysis buffer added (RIPA buffer: PMSF: protease inhibitor cocktail: orthovanadate=100:1:2:1). Cells were then scraped and sonicated for 15 seconds using an ultrasonic homogenizer. Lysate was centrifuged at high speed (13200r/min) for 15 minutes at 4C to pellet the cellular debris. Total protein concentration was determined by a BCA Protein Assay Kit (Pierce). For electrophoresis, protein samples were prepared according to a protein-4x loading buffer (containing DTT) ratio of 3:1, 4x loading buffer containing DTT was diluted with 3 aliquots of protein sample. The sample was mixed and heated at 95C for 5 min, followed by vortex and centrifuge. After running the gel, it was removed from the cassette and assembled inside the Trans-Blot Turbo Transfer System cassette. Transfer was run at 2.5A and 25V for 7mins. The sample was then blocked for at least 1 hour using

5 percent skim milk blocking solution prepared with PBS in RT. Primary FLAG antibody was diluted in PBST with 3 percent skim milk (1:500) and incubated at 4C overnight. The secondary antibody (Licor Anti-Mouse IgG- IRDye 800CW) was diluted in PBST with 3 percent skim milk (1:5000) and placed on a rocker and incubated at RT for 45min. Western blots on Nitrocellulose membranes were scanned using the Odyssey fluorescence scanning system software.

## REFERENCES

- [1] H. Kong *et al.*, “A generalized laplacian of gaussian filter for blob detection and its applications,” *IEEE Transactions on Cybernetics*, vol. 43, pp. 1719–1733, 2013.
- [2] B. Zhang, J. Zerubia, and J.-C. Olivo-Marin, “Gaussian approximations of fluorescence microscope point-spread function models,” *Appl. Opt.*, vol. 46, pp. 1819–1829, 10 Apr. 2007. DOI: [10.1364/AO.46.001819](https://doi.org/10.1364/AO.46.001819). [Online]. Available: <https://opg.optica.org/ao/abstract.cfm?URI=ao-46-10-1819>.
- [3] Richards and Wolf, “Electromagnetic diffraction in optical systems,” *Proceedings of the Royal Society A*, vol. 253, pp. 1358–1379, 1959.
- [4] S. F. Gibson and F. Lanni, “Diffraction by a circular aperture as a model for three-dimensional optical microscopy,” *J. Opt. Soc. Am. A*, vol. 6, pp. 1357–1367, 1989.
- [5] F. Huang *et al.*, “Video-rate nanoscopy using scmos camera-specific single-molecule localization algorithms,” *Nature Methods*, vol. 10, pp. 653–658, 2013.
- [6] R. Nieuwenhuizen *et al.*, “Measuring image resolution in optical nanoscopy,” *Nature Methods*, vol. 10, pp. 557–562, 2013.
- [7] J. Chao *et al.*, “Fisher information theory for parameter estimation in single molecule microscopy: Tutorial,” *Journal of the Optical Society of America A*, 2016.
- [8] T. Dertinger, R. Colyer, G. Iyer, S. Weiss, and J. Enderlein, “Fast, background-free, 3d super-resolution optical fluctuation imaging (sofi),” *Proceedings of the National Academy of Sciences*, vol. 106, pp. 22 287–22 292, 52 2009. DOI: [10.1073/pnas.0907866106](https://doi.org/10.1073/pnas.0907866106). [Online]. Available: <https://www.pnas.org/doi/abs/10.1073/pnas.0907866106>.
- [9] S. Geman and D. Geman, “Stochastic relaxation, gibbs distributions, and the bayesian restoration of images,” *IEEE Transactions on Pattern Analysis and Machine Intelligence*, vol. PAMI-6, pp. 721–741, 6 1984, ISSN: 01628828. DOI: [10.1109/TPAMI.1984.4767596](https://doi.org/10.1109/TPAMI.1984.4767596).
- [10] M. Weigert *et al.*, “Content-aware image restoration: Pushing the limits of fluorescence microscopy,” *Nature Methods*, vol. 15, p. 1090, 2018.

- [11] T. Falk *et al.*, “U-net: Deep learning for cell counting, detection, and morphometry,” *Nature Methods*, vol. 16, pp. 67–70, 2019.
- [12] M. Rust *et al.*, “Sub-diffraction-limit imaging by stochastic optical reconstruction microscopy (storm),” *Nature Methods*, vol. 3, pp. 793–796, 2006.
- [13] E. Betzig *et al.*, “Imaging intracellular fluorescent proteins at nanometer resolution,” *Science*, vol. 313, pp. 1642–1645, 2006.
- [14] W. Ouyang *et al.*, “Deep learning massively accelerates super-resolution localization microscopy,” *Nature Biotechnology*, vol. 36, pp. 460–468, 2018.
- [15] E. Nehme *et al.*, “Deepstorm3d: Dense 3d localization microscopy and psf design by deep learning,” *Nature Methods*, vol. 17, pp. 734–740, 2020.
- [16] A. Speiser *et al.*, “Deep learning enables fast and dense single-molecule localization with high accuracy,” *Nature Methods*, vol. 18, pp. 1082–1090, 2021.
- [17] Y. Song *et al.*, “Score-based generative model through stochastic differential equations,” 2021.
- [18] J. Ho *et al.*, “Denoising diffusion probabilistic models,” 2020.
- [19] B. Lakshminarayanan *et al.*, *Simple and scalable predictive uncertainty estimation using deep ensembles*, 2017.
- [20] Y. Gal *et al.*, “Bayesian uncertainty quantification for machine-learned models in physics,” *Nature Physics*, 2022.
- [21] S. Dirmeier *et al.*, “Diffusion models for probabilistic programming,” 2023.
- [22] F. Ribeiro *et al.*, “Demystifying variational diffusion models,” 2024.
- [23] D. Kingma *et al.*, “Variational diffusion models,” 2021.
- [24] D. Kingma *et al.*, “Understanding diffusion objectives as the elbo with simple data augmentation,” 2023.
- [25] P. Zhang *et al.*, “Analyzing complex single-molecule emission patterns with deep learning,” *Nature Methods*, vol. 15, p. 913, 2018.

- [26] T. H. Kim *et al.*, “Information-rich localization microscopy through machine learning,” *Nature Communications*, vol. 10, p. 1996, 2019.
- [27] P. Zelger *et al.*, “Three-dimensional localization microscopy using deep learning,” *Opt. Express*, vol. 26, pp. 33 166–33 179, 2018.
- [28] C. Saharia *et al.*, “Image super-resolution via iterative refinement,” 2021.
- [29] A. Vahdat *et al.*, “Score-based generative modeling in latent space,” 2021.
- [30] Y. Song *et al.*, “Generative modeling by estimating gradients of the data distribution,” 2019.
- [31] C. S. Smith, N. Joseph, B. Rieger, and K. A. Lidke, “Fast, single-molecule localization that achieves theoretically minimum uncertainty,” *Nature Methods*, vol. 7, pp. 373–375, 5 May 2010, ISSN: 15487091. doi: [10.1038/nmeth.1449](https://doi.org/10.1038/nmeth.1449).
- [32] H. Ta, J. Wolfrum, and D.-P. Herten, “An extended scheme for counting fluorescent molecules by photon-antibunching,” *Laser Physics*, 2010, ISSN: 1054-660X. doi: [10.1134/S1054660X09170204](https://doi.org/10.1134/S1054660X09170204).
- [33] Y. Israel *et al.*, “Quantum correlation enhanced super-resolution localization microscopy enabled by a fibre bundle camera,” *Nature Communications*, vol. 8, p. 14 786, 2017. doi: [10.1038/ncomms14786](https://doi.org/10.1038/ncomms14786).
- [34] J. Goodman and J. Weare, “Ensemble samplers with affine invariance,” *Communications in Applied Mathematics and Computational Science*, vol. 5, pp. 65–80, 1 2010. doi: [10.2140/camcos.2010.5.65](https://doi.org/10.2140/camcos.2010.5.65). [Online]. Available: <https://doi.org/10.2140/camcos.2010.5.65>.
- [35] B. R. Sabari, A. DallAgnese, A. Boija, *et al.*, “Coactivator condensation at super-enhancers links phase separation and gene control,” *Science*, vol. 361, 6400 Jul. 2018, ISSN: 0036-8075. doi: [10.1126/science.aar3958](https://doi.org/10.1126/science.aar3958).
- [36] D. Hnisz, K. Shrinivas, R. A. Young, A. K. Chakraborty, and P. A. Sharp, *A phase separation model for transcriptional control*, 2017. doi: [10.1016/j.cell.2017.02.007](https://doi.org/10.1016/j.cell.2017.02.007).

- [37] J. M. Brown, J. Green, R. P. D. Neves, *et al.*, “Association between active genes occurs at nuclear speckles and is modulated by chromatin environment,” *Journal of Cell Biology*, vol. 182, pp. 1083–1097, 6 Jul. 2008, ISSN: 00219525. DOI: [10.1083/jcb.200803174](https://doi.org/10.1083/jcb.200803174).
- [38] Y. L. Wang, W. W. Zhao, J. Shi, X. B. Wan, J. Zheng, and X. J. Fan, *Liquid-liquid phase separation in dna double-strand breaks repair*, Jul. 2023. DOI: [10.1038/s41419-023-06267-0](https://doi.org/10.1038/s41419-023-06267-0).
- [39] K. Wagh, M. Ishikawa, D. A. Garcia, D. A. Stavreva, A. Upadhyaya, and G. L. Hager, *Mechanical regulation of transcription: Recent advances*, Jul. 2021. DOI: [10.1016/j.tcb.2021.02.008](https://doi.org/10.1016/j.tcb.2021.02.008).
- [40] A. J. Plys and R. E. Kingston, *Dynamic condensates activate transcription*, Jul. 2018. DOI: [10.1126/science.aau4795](https://doi.org/10.1126/science.aau4795).
- [41] A. R. Strom, J. M. Eeftens, Y. Polyachenko, *et al.*, “Interplay of condensation and chromatin binding underlies brd4 targeting,” *Molecular Biology of the Cell*, vol. 35, 6 Jul. 2024, ISSN: 19394586. DOI: [10.1091/mcb.E24-01-0046](https://doi.org/10.1091/mcb.E24-01-0046).
- [42] L. Ma, Z. Gao, J. Wu, *et al.*, “Co-condensation between transcription factor and coactivator p300 modulates transcriptional bursting kinetics,” *Molecular Cell*, vol. 81, 1682–1697.e7, 8 Jul. 2021, ISSN: 10974164. DOI: [10.1016/j.molcel.2021.01.031](https://doi.org/10.1016/j.molcel.2021.01.031).
- [43] T. Wu, Y. F. Kamikawa, and M. E. Donohoe, “Brd4s bromodomains mediate histone h3 acetylation and chromatin remodeling in pluripotent cells through p300 and brg1,” *Cell Reports*, vol. 25, pp. 1756–1771, 7 Jul. 2018, ISSN: 22111247. DOI: [10.1016/j.celrep.2018.10.003](https://doi.org/10.1016/j.celrep.2018.10.003).
- [44] F. Itzen, A. K. Greifenberg, C. A. Bösken, and M. Geyer, “Brd4 activates p-tefb for rna polymerase ii ctd phosphorylation,” *Nucleic Acids Research*, vol. 42, pp. 7577–7590, 12 Jul. 2014, ISSN: 13624962. DOI: [10.1093/nar/gku449](https://doi.org/10.1093/nar/gku449).
- [45] X. Han, D. Yu, R. Gu, *et al.*, “Roles of the brd4 short isoform in phase separation and active gene transcription,” *Nature Structural and Molecular Biology*, vol. 27, pp. 333–341, 4 Jul. 2020, ISSN: 15459985. DOI: [10.1038/s41594-020-0394-8](https://doi.org/10.1038/s41594-020-0394-8).
- [46] P. Filippakopoulos, J. Qi, S. Picaud, *et al.*, “Selective inhibition of bet bromodomains,” *Nature*, vol. 468, pp. 1067–1073, 7327 Jul. 2010, ISSN: 00280836. DOI: [10.1038/nature09504](https://doi.org/10.1038/nature09504).

- [47] S. Y. Wu, A. Y. Lee, H. T. Lai, H. Zhang, and C. M. Chiang, “Phospho switch triggers brd4 chromatin binding and activator recruitment for gene-specific targeting,” *Molecular Cell*, vol. 49, pp. 843–857, 5 Jul. 2013, ISSN: 10972765. DOI: [10.1016/j.molcel.2012.12.006](https://doi.org/10.1016/j.molcel.2012.12.006).
- [48] F. Malvezzi, C. J. Stubbs, T. A. Jowitt, *et al.*, “Phosphorylation-dependent brd4 dimerization and implications for therapeutic inhibition of bet family proteins,” *Communications Biology*, vol. 4, 1 Jul. 2021, ISSN: 23993642. DOI: [10.1038/s42003-021-02750-6](https://doi.org/10.1038/s42003-021-02750-6).
- [49] G. V. Los, L. P. Encell, M. G. McDougall, *et al.*, “Halotag: A novel protein labeling technology for cell imaging and protein analysis,” *ACS Chemical Biology*, vol. 3, pp. 373–382, 6 Jul. 2008, ISSN: 15548929. DOI: [10.1021/cb800025k](https://doi.org/10.1021/cb800025k).
- [50] J. B. Grimm, B. P. English, J. Chen, *et al.*, “A general method to improve fluorophores for live-cell and single-molecule microscopy,” *Nature Methods*, vol. 12, pp. 244–250, 3 2015, ISSN: 15487105. DOI: [10.1038/nmeth.3256](https://doi.org/10.1038/nmeth.3256).